UNIVERSITY OF CALIFORNIA,
IRVINE

Multipolar Raman Scattering on Chiral Plasmons

DISSERTATION

submitted in partial satisfaction of the requirements
for the degree of

DOCTOR OF PHILOSOPHY

in Chemistry

by

Kate Rodriguez

Dissertation Committee:
Professor V. Ara Apkarian, Chair
Professor Matt Law
Professor Eric Potma

2019

DEDICATION

To

my family and friends

in recognition of their continued support.

On being confronted with the unexpected:

“Above all, don't fear difficult moments. The best comes from them."

Rita Levi-Montalcini

Winner of the 1986 Nobel Prize in Physiology or Medicine

TABLE OF CONTENTS

LIST OF FIGURES

Page

Figure 2.3.2 **39**
(a) Transmission electron micrograph image of an isolated dimer formed by two relatively spherical dimers. (b) Prolonged exposure (either to optical or electron beams) reveals a fusing of the two spheres. Plots (c) and (d) show the Raman spectra as a function of time recorded for the linear experiment in the parallel and perpendicular channels, respectively, while a representative spectrum is shown in (e). Several spectral slices are presented here, and the color-coded wings represent the quadrupolar (red) and dipolar (blue) wings of the continuum. Polar plots are presented for the most intense vibrational line, 1640 cm^{-1} (f, g), the blue continuum (h, i), and the red continuum (j, k) in the parallel (left column) and perpendicular (right column) channels. The molecular lines strictly follow the polarization of the dipolar (blue) wing in every case, and do not impart any distinct signature of their own.

Figure 2.3.3 **40**
The results of the linear experiment are presented here for three dimers: D1, of Fig. 2.3.2, as well as two new particles: D2 and D3. (a) While D1 showed clear reflection symmetry in its perpendicular channel response (red trace), (b) D2 and (c) D3 show a broken symmetry that favors either +45° or -45° in their perpendicular channel response (red traces). This effect constitutes linear dichroism.

Figure 2.4.1 **41**
Polarization states generated as a function of the angle the fast axis of the quarterwave plate makes with the original linear polarization, φ. When the two are aligned (φ=0°, 90°, 180°, 270°) the polarization is unchanged. φ=45°,225° generates RCP, while φ=135°,315° generates LCP. At intermediate angles elliptical polarization is generated, with the handedness defined by the CP of that quadrant.

Figure 2.4.2 **42**
Experimental design for the circular dichroism experiments. Linearly polarized light from a continuous wave laser source first passes through a linear polarizer (LP) so that it is oriented along the horizontal. The light is then directed towards a quarterwave plate (QWP, λ/4) at angle φ which induces phase shift e^i2φ between the x- and y-components of the field. After interaction with a single dimer, the backscattered Raman passes through a notch filter (NF) centered at the Rayleigh wavelength, and the full, open-channel signal is recorded.

Figure 2.4.3 **43**
A complete circular dichroism (CD) measurement performed on a single dimer (D3 from Fig. 2.3.3) showing its continuous response as function of the QWP angle, φ. As the dimer is oriented horizontally, the increased response along φ={0°,90°,180°,270°} is due to alignment of the dimer long axis with the linear polarization generated at these angles. The differential scattering along φ=±45° instead reports on the handedness of the antenna. Here, preferential response along φ=-45, which corresponds to LCP, indicates that the dimer is a LH object.

ACKNOWLEDGMENTS

First and foremost, I would like to thank my committee chair and Ph.D. advisor, Professor V. Ara Apkarian, for his continued guidance and support. His open-door policy and willingness to discuss the science, no matter the time or place, was monumentally helpful during my time at UCI.

I would also like to thank my committee members, Professors Matt Law and Eric Potma, for their support and engagement in the contents of this dissertation.

In addition, a thank you to Professors Robbie J. Iuliucci and William Sheers at Washington and Jefferson College for providing me with invaluable research and science communication experience during my undergraduate studies.

I have had the pleasure of collaborating with numerous other graduate students and post-doctorate scholars during my time here at UCI. In particular, I would like to thank Drs. Eero Hulkko and Mayukh Banik for initially training me when I first joined the Apkarian lab. Dr. Banik and I worked very closely on several of the projects presented here, and his continued assistance was invaluable to the success of this work. I would also like to thank Dr. Faezeh Tork-Ladani, whose Comsol simulations provided indispensable theoretical support for several of these projects.

Finally, I would like to acknowledge the center I have been fortunate enough to work under during my entire graduate school career: the NSF-funded Chemistry at the Space-Time Limit (CaSTL). In addition to providing funding for my research (*Award CHE-1414466*), CaSTL has greatly aided my professional and personal development through its many seminars, workshops, and retreats.

CURRICULUM VITAE

Kate Rodriguez

EDUCATION

Doctor of Philosophy in Chemical and Materials Physics **2019**
University of California, Irvine (UCI) *Irvine, CA*

Master of Science in Chemical and Materials Physics **2018**
UCI *Irvine, CA*

Bachelor of Arts in Chemistry **2013**
Washington and Jefferson College (W&J) *Washington, PA*

RESEARCH EXPERIENCE

Graduate Student Researcher **2013-2019**
CaSTL Center, Department of Chemistry, *UCI* *Irvine, CA*

Undergraduate Student Researcher **2010-2013**
Departments of Chemistry and Physics, *W&J* *Washington, PA*

TEACHING EXPERIENCE

Laboratory Assistant **Fall 2013**
Undergraduate General Chemistry

Laboratory Assistant **Winter 2014**
Undergraduate Organic Chemistry I

Teaching Assistant **Spring 2014 & 2015**
Undergraduate Physical Chemistry, Lecture and Lab

Teaching Assistant **Winter 2016**
Graduate Quantum Spectroscopy

ABSTRACT OF THE DISSERTATION

Multipolar Raman Scattering on Chiral Plasmons

By

Kate Rodriguez

Doctor of Philosophy in Chemistry

University of California, Irvine, 2019

Professor V. Ara Apkarian, Chair

Surface-enhanced Raman spectroscopy (SERS) has been an area of active research since its discovery in 1973. In particular, the dimer nano-antenna SERS geometry, consisting of two gold nanospheres functionalized with molecular reporters, has emerged as a powerful and feasible tool for single molecule studies. Despite its popularity, there is still little consensus regrading the role of the nantenna in dictating the observed SERS response. Until issues such as SERS backgrounds, anomalous molecular anti-Stokes intensities, and polarized responses are fully understood, the full power of single molecule Raman can never be realized.

Here, the antenna behavior is clarified via two types of studies: one excitation-dependent study, in which the SERS signal is recorded as a function of increasing laser power, and one polarization-resolved study, in which the SERS response is monitored as a function of changing excitation polarization. Two important discoveries emerge clearly here: first, that the background commonly observed in SERS spectra can be unilaterally assigned to the inelastic light scattering (i.e., Raman) of the plasmon. Second, that the dimer alone dictates the polarization of the scattered response,

including a clear demonstration of both linear and circular chirality. With these in hand, novel applications, such as a quantum description of the plasmon and orientation-dependent chiral response are explored.

INTRODUCTION

Since its discovery in 1973 [1], surface enhanced Raman scattering (SERS) spectroscopy has found near-ubiquitous use, lending itself to applications ranging from the obvious, like single molecule spectroscopy, to more novel techniques including genetic profiling [2] and even cancer diagnostics [3]. Under the application of visible light, the electrons of coinage metals (which are not loosely bound to individual atoms but are rather electron gas-like) collectively oscillate with the alternating field [4]. This collective motion constitutes a plasmon which subsequently mediates the far-field excitation and local molecular interaction.

Though the geometric and material constructions of SERS platforms are nearly as varied as its applications, one of the most fruitful has been the so-called dimer nano-antenna (“nantenna”). The nantenna consists of two gold nanospheres, each ~100 nm in diameter, with ~1 nm interparticle junction populated with a Raman-active molecular reporter(here, bipyridyl ethylene, BPE) [5]. Given that no molecular features are observed on functionalized nanosphere monomers, the nanosphere dimer serves as the simplest construction that allows for single molecule detection. The most critical space of the dimers is in the inter-particle junction (“hot-spot”), where the incident light (~500 nm) is confined down to ~1 nm. The dimer, then, performs the impedance matching between the far-field radiation and molecular reporter. By necessity, due to the small are of the confinement of the field in the hotspot, only one to a few molecules are excited.

Despite its seemingly geometric simplicity, the scattering response of the dimer nantenna is surprisingly rich in both scope and depth. The quantum nature of the

collective electron response of the plasmon, combined with the relatively large scale of the dimer compared to the excitation wavelength ($l \sim \lambda/2$) lead to several interesting phenomena including inelastic intraband light scattering and multipolar Raman of plasmons, both of which are explored in detail below.

Inelastic light scattering on plasmons

SERS on plasmonic structures is invariably accompanied by a background continuum which has been attributed to explanations ranging from fluorescence of the metal [6] to the formation of molecular image charges [7]. This disparity finds clarification here via experiments into the wavelength- and shape-dependence of the SERS scattering response. A clear anti-Stokes portion of the scattering continuum immediately rules out fluorescence, while the appearance of a background on bare metals precludes molecular reasonings. These observations are sufficient to assign the continuum instead to inelastic light scattering on the metal: *i.e.*, Raman of plasmons. While intraband transitions in the metal are typically forbidden due to the orthogonality of the electron *k*-states, this issue can be circumvented through realization that the scattering occurs on the collective state of the plasmon itself.

With this knowledge, the signature of the plasmon can be effectively decoupled from that of the molecule. Further intensity-dependent experiments, which record the SERS response as a function of incident laser power, allow for independent extraction of the molecular and metallic temperatures. While the two are found to be in thermal equilibrium in every case, careful consideration of the intensity profiles reveals an anomaly: both the anti-Stokes and Stokes molecular lines show non-linear intensity

dependence, while the metal remains strictly linear. This observation can only be resolved by including the molecular vibrational partition function in the treatment which, though not necessary in bulk measurements, is apparently crucial in the single-molecule limit.

Multipolar Raman of plasmons

Molecular magnetic and quadrupolar transitions are weak in comparison to dipolar transitions when driven by free propagating optical fields [8]. This is recognized by noting that the ratio of magnetic/quadrupolar to electric dipole transitions $|\langle m\rangle|^2/|\langle d\rangle|^2$ scale as $\zeta^2 = |k\langle r\rangle|^2$, where $k = \frac{\omega}{c} = 2\pi/\lambda$ is the field wave vector and $\langle r\rangle$ is on the molecular length scale. In vacuum, under the long-wave limit, ζ^2~10^{-4} <<1, which allows the spatial dispersion of the electromagnetic waves to be neglected by setting $Ae^{-i(kz-\omega t)} = Ae^{i\omega t}$ in treating light matter interactions [9]. As such, any observation of multipolar vibrational Raman on plasmonic nantennas implies enhancements of order 10^4 beyond the typical SERS enhancement factors of ~10^8. This additional enhancement makes accessible otherwise dark states of matter, including applications such as surface enhanced Raman optical activity (SEROA) and vibrational dichroism, which are otherwise prohibitively weak effects. As the nantenna effectively couples molecular multipoles to the far field, it is crucial to understand the nature of both the metal scattering and molecular coupling mechanisms.

Clearly, the long-wave limit does not apply to such nantennas: at optical wavelengths $l\sim\lambda/2$ and spatial dispersion, or equivalently, retardation effects, cannot be neglected. In addition to dipolar Raman given by the local third order susceptibility, $\chi^{(3)}$,

in which all four field interactions are dipole coupled to the far field, nonlocal response $I^{(3)}$, due to magnetic and quadrupolar contributions, can be seen.

By investigation both the linear and circular dichroism of the nantenna, the response of the dimers can be fully characterized. In every case, the polarization patterns of the molecular lines follow those of the nantenna on which they reside, even when the scattering involves manifestly different multipoles of the molecule and nantenna. The experiments then are ones into plasmonic, rather than molecular, dichroism. Plasmonic chirality, and the subsequent “handedness” of the response, is contrasted against standard molecular chirality in two major ways: first, plasmonic chirality is orders of magnitude larger than its molecular counterpart (parts per ten versus parts per thousand [10]). Second, the handedness is entirely orientation-dependent, whereby a simple in-plane rotation transforms the dimer from a right-handed to a left-handed object.

The observed polarization patterns can be reproduced by expanding local response to second order in spatial dispersion, which contains inseparable terms of electric dipole (d), magnetic dipole (m), and electric quadrupole (q), including the cross terms $< mq >$ and $< md >$ of linear and circular dichroism. In particular, the circular dichroic response md implies excitation of helical plasmons, in which both left- and right-handed behavior is observed on different dimers. That this occurs on the prototypical nano-analog of the Hertzian dipole antenna is remarkable. Both TEM images and theoretical analyses clarify that typical asymmetries in the structure, particularly at the intersphere junction, are sufficient to drive nonlocal response.

Formally, the treatment is formulated in the framework of Jones calculus. It establishes that broken symmetry in the absorption-re-radiation process of the dimers is required to generate the wealth of experimental observations. This treatment, though formulated specifically for the dimers, is entirely general and can be readily extended to any multipolar excitation process. It has important implications in the quantum mechanical treatment of plasmons, including angular momentum states, as well as the general field of bi-isotropic media.

CHAPTER 1: Raman of Plasmons

1.1: Introduction: Backgrounds in Surface Enhanced Raman Scattering

Plasmonic nanostructures are extensively used as nano-antennas (nantennas) to couple far-field radiation to molecular receivers [11]. Their ability to confine light beyond the diffraction limit to the nm scale allows for the generation of large, highly localized fields. This confinement constitutes the physical mechanism of surface enhanced Raman scattering (SERS) [12, 13] under which single molecule sensitivity can be achieved [14-19]. One of the more commonly used designs for these purposes is the nanosphere-dimer – two metallic nanospheres adjoined by molecular linkers. As the nano-analog of the Hertzian dipolar antenna, the nanosphere dimer has been subjected to extensive experimentation [20-25] and theoretical analysis [26-32]. This constitutes the simplest prototype of a nano-junction which plays a two-fold role: in addition to generating enhanced field confined at the gap (hot-spot), it also broadcasts the spectroscopic signature of reporter molecule(s) present in the junction. We find that junction dynamics – in terms of morphology and evolution, which are difficult to control or characterize experimentally – dictates to significant extent the resulting SERS spectra. As the highest local fields are generated in the plasmonic junction, a rich tapestry of photophysics is generated in this sub-nm critical space, including charge transfer and quantum effects such as tunneling plasmons [33-35]. Recently, nearly exact ab-initio theoretical calculations have illustrated the importance of atomic scale structural variations in determining plasmonic response of sodium nano-dumbbells [36]. Experimental observation of photophysics on a real plasmonic junction was highlighted

in a study of SERS on a single silver dumbbell undergoing light-induced fusion [23]. There, magnetic and quadrupolar SERS, charge transfer plasmon-driven Raman, and rectification [37] of photocurrent through Stark shifted Raman were identified. These observations have important implications with regards to molecule-plasmon interactions and, more importantly, emphasize the crucial role of the antenna in general and the junction in particular in dictating far-field scattering response.

In this chapter, a straightforward model for the background continuum observed in the SERS spectra is presented. While a variety of inelastic scattering processes may contribute to the background in different experimental arrangements, the continuum observed here can be assigned predominantly to electronic Raman scattering on the metal. Through exhaustive experimentation, the scattering nature of plasmonic nantennas will be directly extracted from the spectra themselves. The intensity profiles of the anti-Stokes tail is used to extract electronic temperature of the metal, while comparison of the Stokes and anti-Stokes molecular vibrations is used to determine the vibrational temperature of the molecule. After rigorous analysis, it appears that the molecule (including all vibrations) is generally in equilibrium with the metal temperature up to threshold under which no permanent damage is incurred. The method described here serves as a reliable nanothermometer, providing a realistic temperature gauge for the hotspot, the most critical functional space of the plasmonic junction.

1.2: Experimental

SERS spectra are recorded on individual gold nanosphere monomers and dimers onto which molecular reporter bipyridyl ethylene (BPE) is adsorbed. Particles with average diameter 90 ± 5 nm are encapsulated in a silica shell (~70 nm thickness), a size where radiation competes with the dephasing of surface plasmons. Scanning and tunneling electron micrographs allow for identification and characterization of the particles of interest, which are analyzed individually. Spectra are collected using 532 (diode-pumped solid state) and 633 (He-Ne) nm laser excitation, in the backscatter geometry with high NA microscope objective (NA = 0.625) and a notch filter with a rejection band of ±250 cm-1 centered at the respective Rayleigh line. For intensity-dependent measurements, the incident laser power was increased from 0.1to 1.7 mW/μm^2 (633) or ~1 mW/μm^2 (532) in steps of roughly 0.1 mW/μm^2. In all cases, the laser intensity was carefully controlled via a neutral density filter (NDF) placed just after the laser source (Fig. 1.2.1).

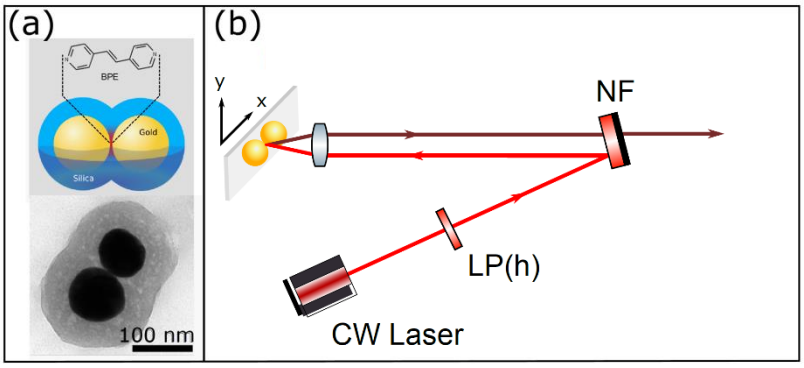

Figure 1.2.1. (a) Schematic and transmission electron micrograph of a typical dimer. (b) Experimental geometry. The intensity of a CW laser source is controlled via a neutral density filter (NDF). A notch filter (NF) centered at the excitation wavelength is used as a mirror to direct the source toward a single dimer. After interaction, the backscattered Raman is filtered through the NF and the signal is dispersed onto the detector for analysis.

1.3: Results: SERS on Metallic Structures

Despite the extensive attention devoted to plasmonic junctions in the past few decades, the origin of the background that invariably accompanies their SERS spectral response remains the subject of deliberation [38-44] and unanimous agreement is yet to be achieved. Though it has been increasingly recognized to be arising from metallic response, it has been separately attributed to both metallic photoluminescence due to radiative recombination [43] and intraband scattering processes [45]. To first verify that the origins of the continuum are metallic in nature, the SERS spectra obtained on a variety of gold substrates is presented in Fig. 1.3.1a: nanoparticle monomer, nanoparticle dimer lacking molecular reporter, and evaporated gold substrate. Each of these systems is bare, lacking any molecular functionalization, yet they all show a clear, continuous background, precluding its assignment to a consequence of molecular image charges [7]. To argue that the continuum is due to the collective plasmon rather than individual, incoherent electron transitions, the results of polarization-resolved experiments are presented in Fig.1.3.1c-d. A thorough discussion of the polarized scattering nature of the antenna will be reported in Chapter 2; here it is noted only briefly that the Stokes scattering response is highly polarized along the antenna long axis, indicating that the scattering is coherent, and is aware of the structure and orientation of the object. Such polarized response indicates coherent luminescence, which is equivalent to resonant Raman. Although gold does have a broad interband transition centered at 2.4 eV (520 nm) [46], incoherent luminescence implies dephasing either through electron-electron or electron-phonon collisions prior to emission, which

will scramble the polarization. Finally, the appearance of a clearly exponentially decaying anti-Stokes decaying tail in all cases (Fig. 1.3.1b) further clarifies that the continuum cannot arise from interband processes, as they do not allow for emissions at energies higher than the excitation.

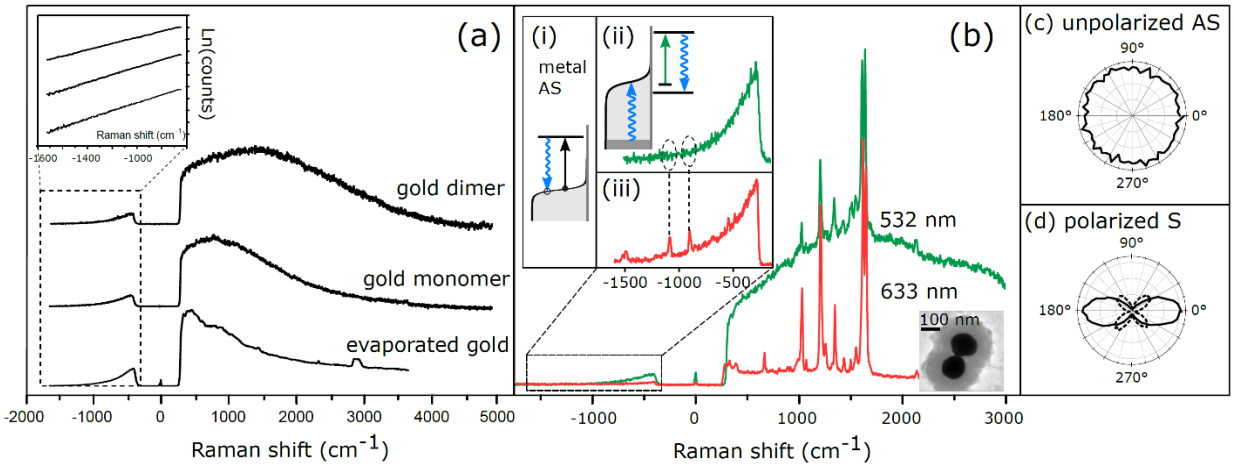

Figure 1.3.1. a) Raman spectra collected on a variety of metal structures, including a gold nanodimer (200 nm diameter), gold nano-monomer (100 nm diameter), and evaporated metal film. All samples are free of molecular reporters, indicating that the broad continuum can only arise from inelastic light scattering from metallic electrons. While the Stokes signatures vary between the three structures, each shows an identical decaying tail in the anti-Stokes (AS) regime. The exponential nature of this tail is highlighted by the linear plots obtained from semi-log plots (inset). (b) SERS spectra collected on a gold nanodimer functionalized with molecular reporter bipyridyl ethylene (BPE) under both 532 nm (green) and 633 nm (red) excitation. In addition to the increased metallic background response excited at 532 nm compared to 633, it also conspicuously lacks any molecular AS peaks regardless of the laser intensity. We attribute this to the metallic reabsorption of emitted AS photons which are harmonious with gold's d → s interband excitation. (c) Polarization-resolved experiments reveal that only the Stokes region yields is polarized.

1.3.1: SERS of bare metals

In Fig. 1.3.1a, the Raman spectra of three distinct metal structures are presented: a bare (molecule-free) gold dimer, a bare gold monomer (100 nm diameter), and a standard bare evaporated gold film. In each case, the spectra exhibit a broad continuum that persists through the entire spectral range. The Stokes side reveals that the spectral composition depends to large extent on the geometry of the metal. More detail on the various resonances that decorate the Stokes side are given in Chapter 2. Here it is noted only that this continuum is general and can only arise as a consequence of metallic scattering.

Interestingly, each spectrum presented in Fig. 1.3.1a shows an identical, exponentially decaying anti-Stokes (AS) tail. The pure exponential nature of these tails is emphasized by the semi-log plot inset, which reveal clear linearity for as long as the signal remains above the noise level. This AS Raman branch will be the point of interest for the remainder of the paper.

1.3.2: SERS of functionalized nantenna

Fig. 1.3.1b presents two representative cases of SERS obtained from a single dimer under 532 nm (green) and 633 nm (red) CW excitation. In both cases, the discrete molecular vibrations from the molecule, bipyridyl ethylene (BPE), appear on top of the broad Stokes continuum of the metal. The Stokes assigned primarily to plasmon resonances because to their strong polarization (Fig. 1.3.1c-d). The large (~3000 cm^{-1}) spectral width evident particularly under 532 nm is indicative of typical plasmon decay times on the order of 10 fs. While the difference in the shape of the continua arise from

the uniquely excitable plasmon modes, the variation in intensity of the scattering background relative to the molecular lines can be associated with the spectral dependence of the penetration depth of gold: 45 nm at 532 nm excitation, versus 30 nm at 633 [47]. Generally, the metal-molecule scattering ratios, calculated from dozens of dimers analyzed, are found to be 1:1 for green and 1:10 for red. This claim is further validated at 785 nm excitation, where the penetration depth of gold is lowered to ~25 nm and the SERS response is virtually background-free.

The origin of the AS regime is quite different, as first indicated by the entirely isotropic nature of the signal (Fig. 1.3.1c). Moreover, the characteristic decay is maintained as a function of excitation wavelength, nullifying any arguments of resonant contribution in the underlying mechanism. Interestingly, there is no evidence of molecular anti-Stokes under 532 regardless of excitation intensity, which we ascribe to interband reabsorption of the emitted photon (Fig. 1.2.1b, ii). Here, the blue-shifted AS photons are now energetic enough to match the 2.5 eV d→s interband transition in the metal and so are immediately reabsorbed. The less energetic 633 nm AS emission does not reach the interband resonance and hence molecular AS vibrations, which are no longer in competition with metallic absorption channels, are observed.

1.4: Results: Laser Intensity-Dependence Studies

To better understand the behavior of the metallic and molecular scattering, dimers are subject to laser intensity-dependence studies. The results of such a study for an individual dimer, D1, is presented here under both 532 (Fig. 1.4.1) and 633 nm (Fig. 1.4.2) excitation, for four illustrative powers. There are a few marked differences in the power series data between the two colors, in addition to the lack of molecular AS under 532 nm excitation. In the case of 633 nm excitation, even relatively high laser powers produce nearly identical, clean molecular spectra. Under 532 nm, however, the molecular lines begin to broaden and eventually fuse >~500 μW/μm^2, while the metallic background develops additional humps not observed at lower powers. In some cases, the degradation of the molecular signal is entirely reversible, while in others it remains permanent. Accordingly, the exact origins of this phenomenon are likely varied, with possibilities such as irreversible molecular degradation and reversible metal-molecule Fano coupling [48] likely both playing a role. In any case, if the incident intensity under 532 nm is raised above ~1500 μW/μm^2, the dimer itself is destroyed. Under 633 nm, on the other hand, even full laser intensity (1700 μW/μm^2) does not induce any damage to the metal or molecule. Apparently, the two excitation colors lead to drastically different heating effects in the nantenna, which will be explored in the proceeding sections.

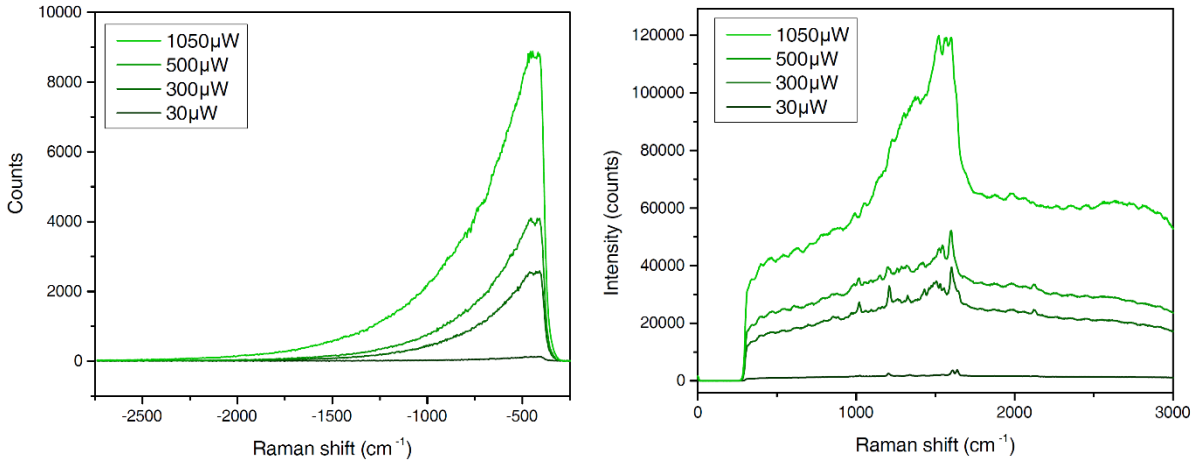

Figure 1.4.1. Results of a laser intensity-dependence study performed on a dimer, D1, under 532 nm CW excitation. The anti-Stokes regime (left) is free from any molecular signature regardless of incident excitation intensity. The Stokes regime (right) often shows a broadening and eventual merging of molecular lines, which in this case was irreversible. Additionally, the background continuum develops resonances (~2800 cm^{-1}) not observed at lower powers. In this case, the bumps likely developed as a consequence of fusing of the individual spheres.

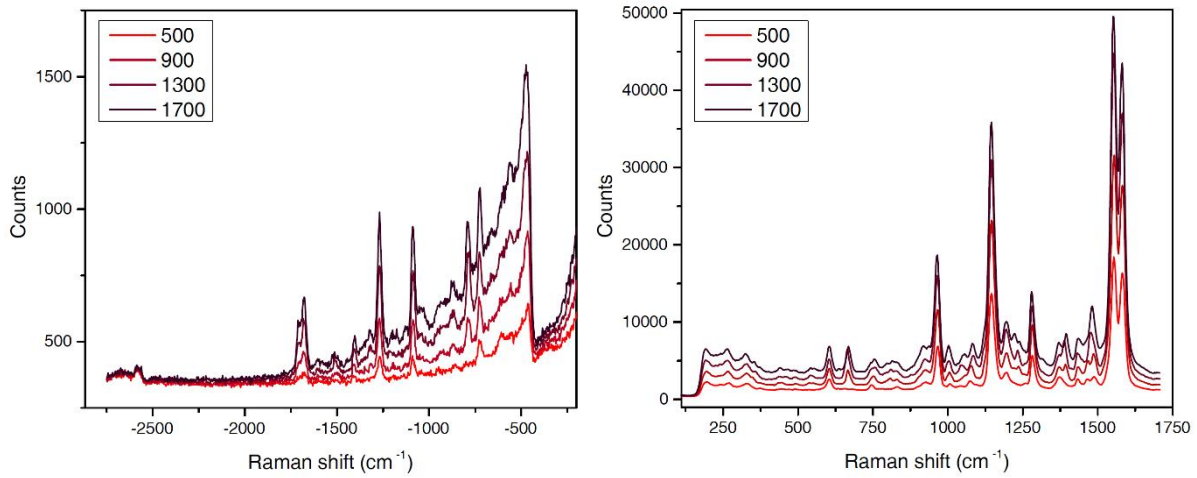

Figure 1.4.2. Results of a laser intensity-dependence study performed on a dimer, D1, under 633 nm CW excitation. The anti-Stokes regime (left) shows clear molecular signatures in all instances, though the signal becomes clearer at high powers. The Stokes regime (right) remains nearly identical over the course of the measurements.

1.5: Molecular Temperature

Information on molecular (vibrational) temperature is extracted from the ratio of the intensity of the anti-Stokes to Stokes lines. Correspondingly, the lack of molecular AS at 532 nm precludes its inclusion here, and so only 633 nm data is used. Six vibrations in total were chosen for the analysis, which are defined as follows.

Vibration	Wavenumber (cm^{-1})
Vib 1	1641
Vib 2	1604
Vib 3	1200
Vib 4	1008
Vib 5	738
Vib 6	663

Table 1.5.1. List of the molecular vibrations used in the temperature analysis with their corresponding shorthand notations.

The ratio of anti-Stokes to Stokes intensities (I_{AS} and I_S, respectively) as a function of incident laser and vibrational frequencies ($\bar{\nu}_L$, $\bar{\nu}_{vib}$, in wavenumbers) is given by:

$$\frac{I_{AS}}{I_S}\left(\frac{\bar{\nu}_L-\bar{\nu}_{vib}}{\bar{\nu}_L+\bar{\nu}_{vib}}\right)^3 = e^{-\bar{\nu}_{vib}/kT}. \qquad 1.5.1$$

Here, the cubed power term arises from the vacuum density of states. Accordingly, the anti-Stokes data is scaled by $(\bar{\nu}_L - \bar{\nu}_{vib})^3/{\bar{\nu}_L}^3$ while the Stokes by $(\bar{\nu}_L + \bar{\nu}_{vib})^3/{\bar{\nu}_L}^3$. For a shift occurring around $\bar{\nu}_{vib}$ =1640 cm^{-1}, this correction scales the anti-Stokes line by a factor of 0.72 and the Stokes by 1.34. For the molecule, each vibration is weighted by its singular Raman shift $\bar{\nu}_{vib}$ in this way, while the metal correction will be done for the continuum. That the correct correction be done is crucial: If left untreated, the data will

yield artificially high temperatures due to the preferential weighting of the anti-Stokes shifts.

Extraction of vibrational temperature from Eqn. 1.5.1 proceeds straightforwardly. When carried out for dimer D1, all six vibrations yield similar temperatures at each incident intensity, revealing that the vibrations are in thermal equilibrium as expected. Additionally, extraction to zero-intensity yields temperatures at or near 300K (Fig.1.6.2).

For dimer D1, as well as several others analyzed, both the Stokes and anti-Stokes lines show clear non-linear intensity dependence (Fig. 1.5.1). This is most apparent as the laser intensity surpasses ~1200 μW/μm^2 – here, the Stokes lines plateau while the anti-Stokes rapidly increase. Linear fits return substantial y-intercepts (positive for Stokes, negative for anti-Stokes), on the order of 20% of the median counts. Even if these higher powers are ignored, the intercepts (while reduced to ~15% of the median counts) remain non-zero and the residuals are significant.

To account for the observed nonlinearity, the molecular vibrational partition function for BPE is utilized. Each normal mode of BPE will contribute to the total partition function. Under the harmonic approximation (and setting the ground state energy to zero), the vibrational partition function is given by the product of each mode $\bar{\nu}$:

$$Q = \prod_{\bar{\nu}} \frac{1}{1-e^{-\bar{\nu}/kT}}. \qquad 1.5.2$$

The partition function describes the distribution of the population into the thermally accessible vibrational states. Its inverse, $1/Q$, accordingly describes the depletion of the ground (zero-energy) state into the higher energy vibrational states and serves as the normalization constant. Both Q and $1/Q$ are shown as a function of temperature in Fig. 1.5.2.

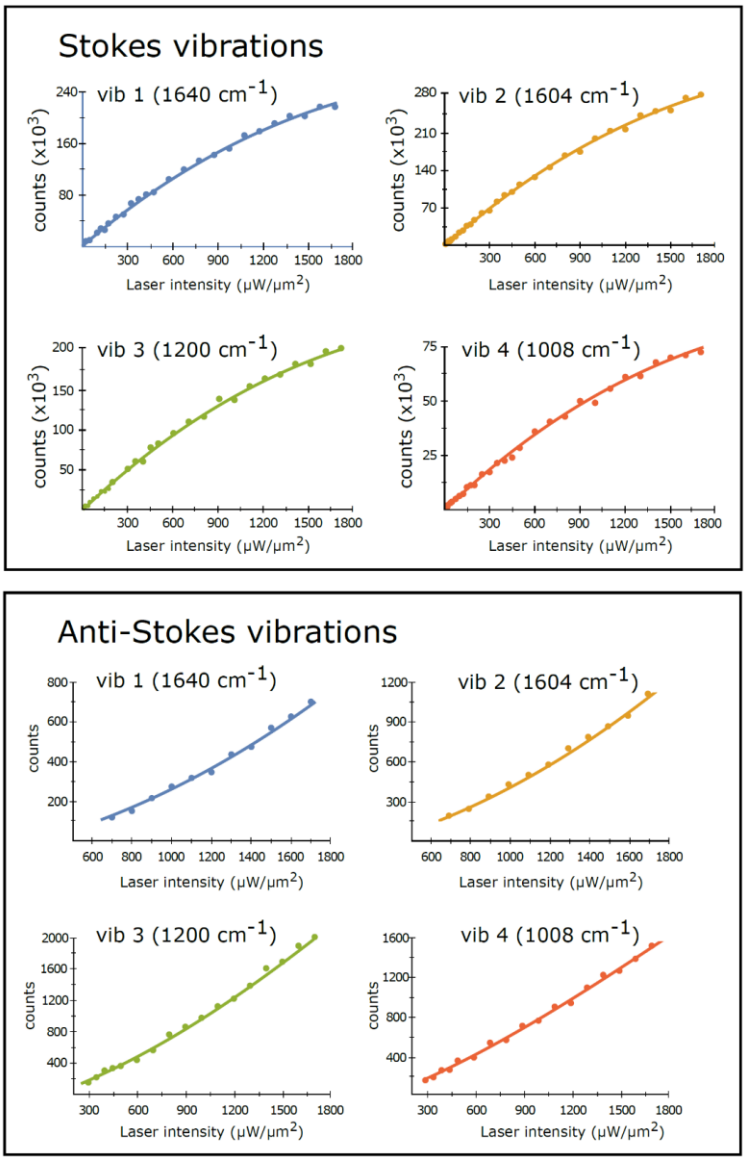

Figure 1.5.1. Stokes (top set) and anti-Stokes (bottom set) line counts as a function of laser intensity for four vibrations of interest. Both show highly non-linear response, an effect which has been reproduced across a number of dimers.

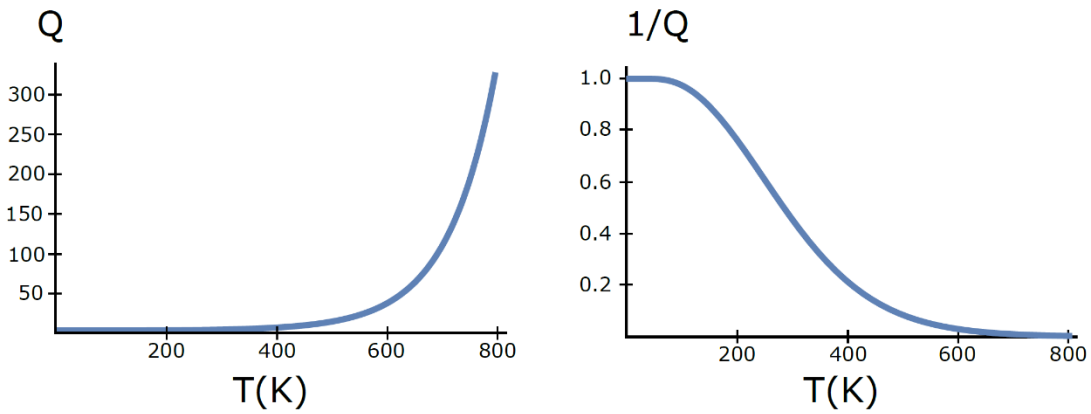

Figure 1.5.2. The partition function Q (left) and its inverse $1/Q$ (right) as a function of temperature. While Q describes the spread of the population into available vibrational states, $1/Q$ according reports on the depletion of the ground state.

As any Stokes scattering process is proportional to the ground state population, it is therefore expected that all Stokes vibrations will follow basic $1/Q$ dependence. The anti-Stokes, on the other hand, is limited instead by the population in the initial vibrationally excited state. As such, it depends highly on the mode of interest (v_{AS}). The two processes, Stokes (S) and anti-Stokes (AS) are then succinctly described as follows,

$$I_S(T) \propto c_v \frac{1}{Q(T)} \quad 1.5.3$$

$$I_{AS}(T) \propto c_v \frac{e^{-\frac{\bar{\nu}_{AS}}{kT}}}{Q(T)} \quad 1.5.4$$

where c_v is the cross-section of each vibration. To recast these descriptions in terms of intensity I, the average of the heating rates presented in Fig. 1.6.2 can be used, replacing $T \rightarrow T_0 + \Delta T_{avg} * I = T_0(K) + 0.055\ K/\mu W * I(\mu W)$, and the overall functions multiplied by I as follows.

$$Q(I) = \prod_{\bar{\nu}} \frac{1}{1-e^{-\bar{\nu}/k(300+0.055*I)}} \quad 1.5.5$$

$$S \propto c\, I \frac{1}{Q(I)} \quad (1.5.6)$$

$$AS \propto c' I \frac{e^{-\bar{\nu}_{AS}/k(300+0.055*I)}}{Q(I)} \quad (1.5.7)$$

The modes used to calculate Q were taken from [49]. For the fits (solid lines present in Fig. 1.5.1), all 58 calculated frequencies (A_g, B_g, A_u, and B_u) were used. Parameter c_v is left as a free parameter in the fit.

The curvature present in the intensity-dependent plots of Fig. 1.5.1 are only describable under this partition function treatment. Previous arguments of phenomena such as vibrational pumping in SERS [50], which result in quadratic AS intensity-dependence, are not suitable here. Firstly, the S lines in the dimers do not remain linear across the range of the measurements, as is standard in the case of pumping, and which was observed in [50]. Secondly, quadratic fits do not sufficiently describe the AS data in Fig. 1.5.1: though the fits look reasonable at first glance, they return extremely large zero-power counts (y-intercepts) and a negative x^1 parameter (Fig. 1.5.3).

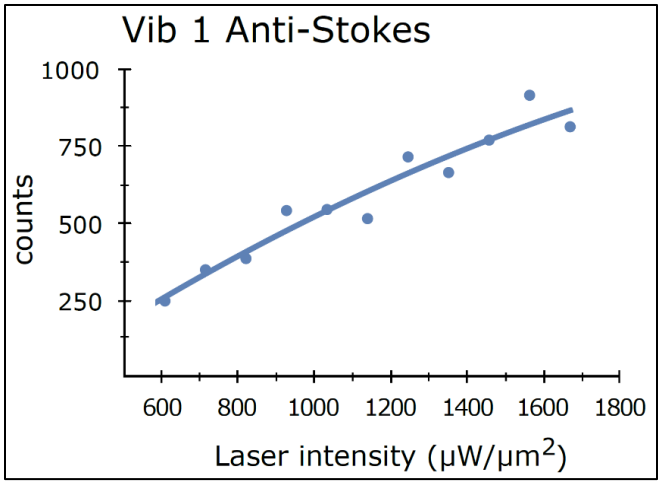

Figure 1.5.3. Quadratic fit to the Anti-Stokes intensity-dependence of a different dimer, for vibration 1 (1640 cm^{-1}). Though quadratic fits appear at first glance to describe the laser intensity-dependence of the anti-Stokes vibrations, two issues arise upon closer inspection. First, extrapolation to zero laser power, which should return zero counts, give artificially large values (up to 66% of the median counts in the series here). Furthermore, fits to the function $f(x) = ax^2 + bx + c$ consistently return a negative b parameter.

1.6: Metallic Temperature and Comparison with the Molecule

To extract metallic temperature, the anti-Stokes decaying tail is fit to the Fermi Dirac distribution (with ω^3-correction):

$$f(\bar{\nu}) = \left(\frac{\bar{\nu}_L}{\bar{\nu}_L+\bar{\nu}}\right)^3 \left(\frac{A_0}{1+e^{-\frac{\bar{\nu}}{kT}}}\right) + y_0 \qquad 1.6.1$$

where the sign reversal in the exponential flips the function to match the direction of decay of the anti-Stokes tail. The spectra shown in the power-dependence results of Figs. 1.4.1 and 1.4.2 have been baseline corrected, which is commonly performed by finding the absolute minimum in spectral intensity, and subtracting this value from all other points. This process poses a unique problem for the exponential tail: introduction of a constant offset, whether positive or negative, will introduce an artificial curve in the resulting semi-log plot. To correct for this, the anti-Stokes region is separated into two equally sized cuts. For example, for dimer D1, the full spectral AS range corresponds to two cuts, the first from -2750 to -1520, and the second from -1520 to -440. Cut 1 is then

shifted to the same spectral range as Cut 2, and subtracted from it. This process effective corrects for any artificial offset in the data, and is illustrated in Fig. 1.6.1 for D1 under 532 nm, where the lack of molecular AS makes the interpretation clear.

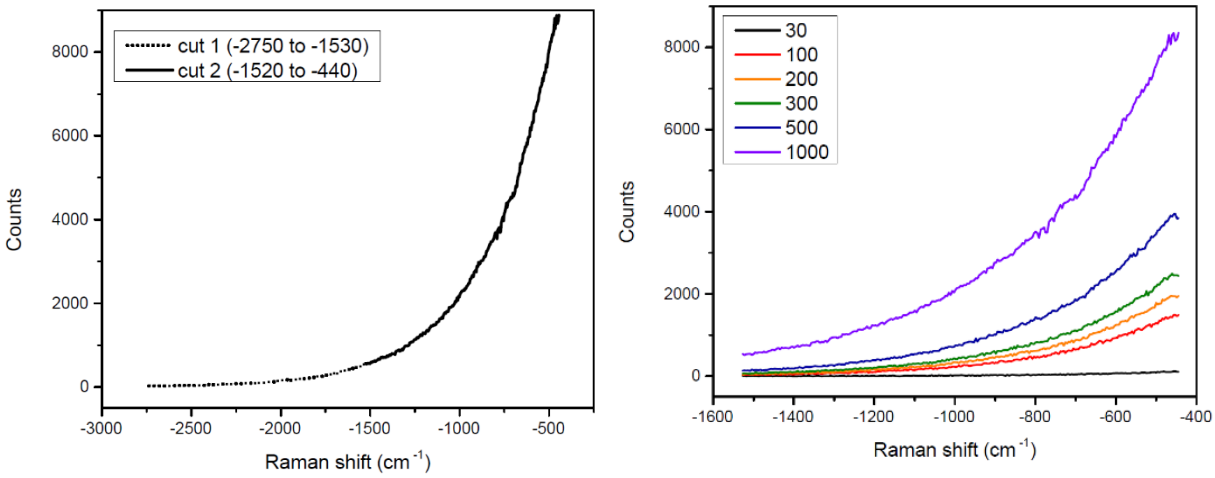

Figure 1.6.1. Left: The shift-and-subtract method of eliminating constant offsets in the anti-Stokes exponential decay, as illustrated for dimer D1. The left plot shows the two cuts the region is separated into; cut 1 is then shifted to match the spectral region of cut 2, and subsequently subtracted from it. Right: The resulting shifted-and-subtracted AS tails for six representative powers in the series.

The resulting metallic temperature extracted in this way for D1 under 633 nm is also shown in Fig. 1.6.2, and it is noted that zero-power extrapolation yields a realistic temperature of 312± 10K. As earlier alluded to, it is evident that the dimers heat up substantially faster under 532 nm. Unfortunately, the lack of 532 nm molecular AS signal prevents the use of the molecular thermometer, but treatment of the metal alone yields a heating rate of nearly double that of 633 nm, at ~0.9 K/μW/μm^2.

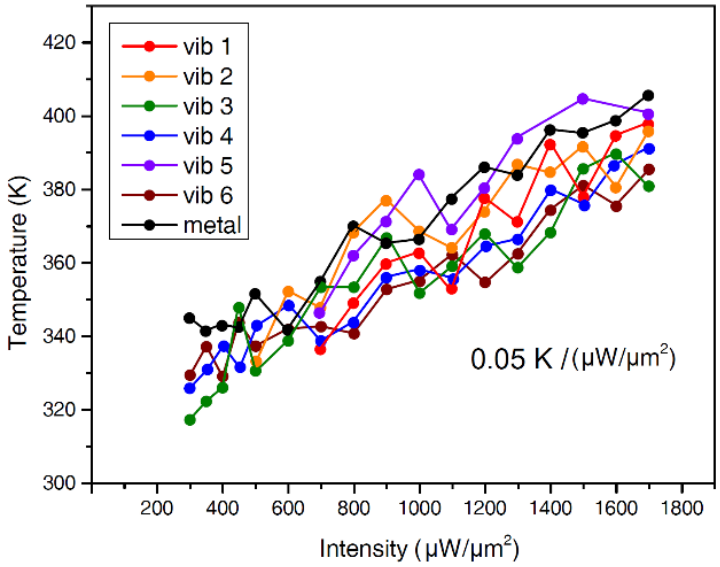

	Intercept	Slope (K/μW)
Vib 1	298± 10K	0.054
Vib 2	297± 10K	0.056
Vib 3	296± 10K	0.055
Vib 4	302± 10K	0.055
Vib 5	299± 10K	0.056
Vib 6	303± 10K	0.054
metal	312± 10K	0.058

Figure 1.6.2. Extracted temperatures for the six molecular vibrations of interest from dimer D1, according to Eqn. 1.5.1. When the requisite ω^3-correction is implemented, all vibrations yield zero-intensity intercepts at or around room temperature. Furthermore, the metal (black trace) is shown to be consistently in thermal equilibrium with all molecular vibrations.

It has long been standard to employ a ω^4-correction to the data, rather than the ω^3-correction used here. The reason for deploying ω^3 is two-fold. First, it more accurately describes the way modern measurements are made. While ω^4-corrections are appropriate for energy-based detection methods, any photon counting collection methods (such as the CCD detector used herein) require instead ω^3-corrections. Secondly, using ω^3 leads to more physically meaningful temperature values. Under ω^3, all extrapolations to zero-intensity yield temperatures at or around room temperature (±~10K), while ω^4-corrected data consistently runs ~15K colder, leading to sub-300K temperatures at zero laser intensity.

1.7: Mathematical Formulation: Electronic Raman Scattering

While a formal description of the ERS of the metallic plasmon is squarely rooted in quantum mechanics, it can be rationalized via the straightforward formulation presented below. For simplicity, the derivation is presented in one dimension, at a single metal-vacuum interface. Extensions to bare (metal-vacuum-metal) and functionalized (metal-molecule-metal) geometries follow naturally from this treatment. Here, the background is attributed to the inelastic electronic scattering of the metal, mediated by the collective charge density oscillations of the plasmon. This process is realized through intraband electronic transitions, which are typically disallowed due to the orthogonality of the bulk momentum (*k*-) states of the individual electrons [45]. Here, however, there is a simple but critical distinction. Rather than individual intraband electron scattering events, in which an electron within the s-band is promoted to an unoccupied intermediate hole state before relaxing into a final s-band hole state, the ERS is facilitated directly by the collective, multi-electron plasmon state. The plasmon is comprised of individual electron states and so each comprising state necessarily has a non-zero projection into the collective plasmon wavefunction (*e.g.*, the states are no longer orthogonal).

It is well understood that at the optical frequencies of interest, particularly where the dielectric response is negative, the limited penetration depth of electromagnetic fields into metals immediately implies that the standard Raman effect will be feeble and instead dominated by scattering on collective charge density oscillations. In contrast with shape-determined elastic light scattering spectra, which are adequately described under classical electrodynamics, the inelastic ERS process is quantum mechanical in

origin. As such, this background is expected to probe the sought-after quantum aspects of the surface plasmons, a phenomenon which is further elaborated on in this section.

1.7.1 Describing the plasmon

For a plasmonic surface charge density, we are only interested in the charge distribution (σ_s) across the metal-vacuum junction, *i.e*., normal to the metal surface (along $\hat{z}$):

$$\sigma_s = \delta n(r_\perp) = \delta n(z) = {\varphi_{pl}}^*(z) \cdot \varphi_{pl}(z), \tag{1.7.1}$$

which is described in terms of the differential charge, $\delta n(z)$, across the interface. This is recast in terms of the of the plasmonic wavefunction $\varphi_{pl}(z)$, the square modulus of which determine charge distribution. To calculate the plasmon wavefunction explicitly, we recognize that the plasmon is simply the response of the metal to the applied field ($F = ezE$):

$$\delta n(z) = n_{F=0} - n_{F=ezE} = {\varphi_{pl}}^* \varphi_{pl}|_{F=0} - {\varphi_{pl}}^* \varphi_{pl}|_{F=ezE}. \tag{1.7.2}$$

This is done numerically using the relevant parameters of gold (Fermi level, work function, *etc*.): the wavefunctions in both the unperturbed ($F = 0$) and perturbed ($F = ezE$) cases are determined by solving their respective Hamiltonians and the difference density computed. Qualitatively, the application of the field bends the potential barrier causing a redistribution of electron *k*-states that becomes particularly pronounced at higher energies. As the plasmonic charge density is a result of all participating electrons, it can be decomposed into its individual electron components:

$$\delta n = \left|\varphi_{pl}(z)\right|^2 = \left|\sum_i a_i \psi_i(E)\right|^2 \tag{1.7.3}$$

where a_i are the coefficients that weight the contributions of each single electron wavefunction $\psi_i(E)$ into the collective plasmon state φ_{pl}. The plasmon is generated from optically accessible states from E_F down to $E_F - E_{excitation}$:

$$\tilde{\varphi}_{pl}(z) \approx \int_{E_F - E_{exc}}^{E_F} a(E)\psi(E,k)\, dE \qquad 1.7.4$$

where it is recognized that the density of electronic states in a metal approaches a continuum. The form of $a(E)$ can now be computed from $\tilde{\varphi}_{pl}$ and $\psi(E,k)$, which are just the electron Bloch states. The computed $\delta n(z)$ and projections $a(E)$ are shown in (Fig. 1.7.1a. It is found that the weighting coefficients depend exponentially on the difference in energy between the state and the Fermi, Δ (Fig. 1.7.1b):

$$a(E) \approx N e^{\frac{E}{\Delta}}. \qquad 1.7.5$$

From here, the Raman scattering process can now be formulated via the collective plasmonic wavefunction.

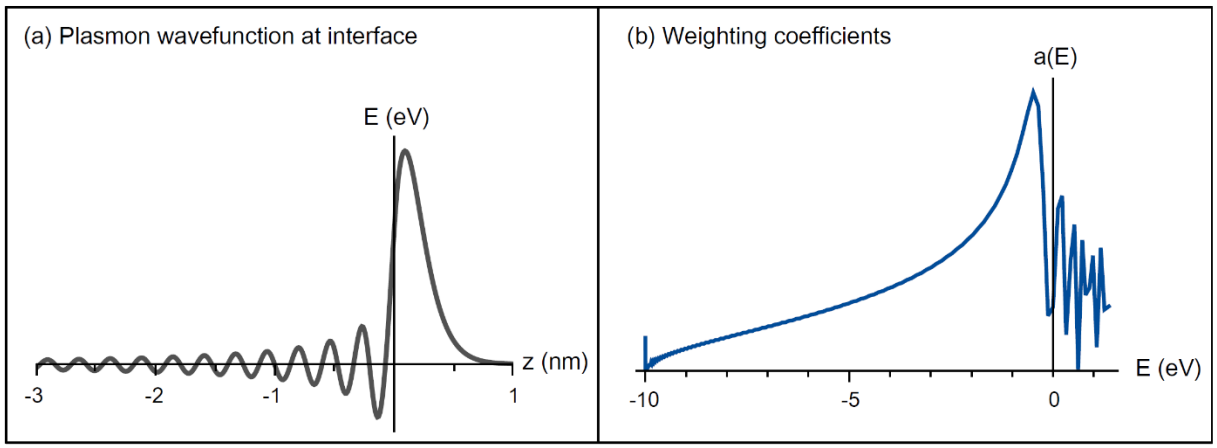

Figure 1.7.1. (a) The wavefunction of the plasmon generated at a metal-vacuum interface (z=0), $\delta n(z)$, computed by subtracting the electron density generated under the applied field from the unperturbed density. (b) The weighting coefficients, $a(E)$, which give the projections of the single-particle states onto the collective plasmon wavefunction.

1.7.2: Describing plasmonic Raman scattering

Mathematically, non-resonant Raman scattering processes are conveniently expressed in the for of Fermi's Gold Rule for transition rates between discrete states:

$$W(\omega_{is}) = \frac{2\pi}{\hbar}\left|\langle f|\hat{V}|i\rangle\right|^2 \delta[(\hbar\omega_i - \hbar\omega_s) - (E_i - E_F)]. \qquad 1.7.6$$

Consider just the matrix element $\langle f|\hat{V}|i\rangle$, which determines the nature of the states that participate in the scattering process. In the ERS process, an electron starts in an occupied electron state (e) and, through participation in the collective plasmon oscillation, ends up in an available hole state (h):

$$\langle f|\hat{V}|i\rangle = \langle h|\tilde{\varphi}_{pl}\rangle\langle\tilde{\varphi}_{pl}|e\rangle. \qquad 1.7.7$$

This subtle distinction is the crux of the intraband transition model presented here. Rather than a separate *k*-state serving as an intermediate for the transition, which is

prohibited due to the orthogonality of Bloch states $\langle e_j|e_i\rangle = 0$, the electron is projected directly into the plasmon state with which it has non-zero overlap.

The states of Eqn. 1.7.7 can be recast in terms of their energy given that the electron starts at state E and scatters into a final state of $E + \varepsilon$ (where ε may be positive or negative for Stokes and anti-Stokes processes, respectively). Also note that the "dressed" plasmon state $\tilde{\varphi}_{pl}$ is simply φ_{pl} under the application of an external field to write:

$$\langle h|\tilde{\varphi}_{pl}\rangle\langle\tilde{\varphi}_{pl}|e\rangle = \langle E+\varepsilon|\hat{V}|\varphi_{pl}\rangle\langle\varphi_{pl}|\hat{V}|E\rangle. \quad 1.7.8$$

The field-induced potential is of the form $\hat{V} = ezE = A \cdot p = -i\hbar A \cdot \frac{\partial}{\partial z}$. The final form here will be particularly useful as the electron states of $\tilde{\varphi}_{pl}$ are unperturbed, given in terms of their Bloch functions, $\psi \sim e^{ikz}$ – here, the action of the momentum operator will simply pick out *k*. Additionally, in the long-wave limit, $A \to A_0 \equiv constant$. This reduces the matrix element to

$$\langle E+\varepsilon|\hat{V}|\varphi_{pl}\rangle\langle\varphi_{pl}|\hat{V}|E\rangle = \hbar^2 A_0^2 k(E)k(E+\varepsilon)\langle E+\varepsilon|\varphi_{pl}\rangle\langle\varphi_{pl}|E\rangle. \quad 1.7.9$$

The terms $\langle E+\varepsilon|\varphi_{pl}\rangle$ and $\langle\varphi_{pl}|E\rangle$ project the plasmon back into the individual electron states and are therefore simply the weighting functions, $a(E+\varepsilon)$ and $a(E)$:

$$\langle E+\varepsilon|\varphi_{pl}\rangle\langle\varphi_{pl}|E\rangle = N^2 \int e^{(E+\varepsilon)/\Delta} e^{E/\Delta} dE \quad 1.7.10$$

which is nothing more than a correlation of the form $e^{-|\varepsilon/\Delta|}$. This matrix element can now be plugged back into Fermi's Golden Rule (Eqn. 1.7.6) along with the relative electron/hole density of states expressions ρ_e/ρ_h and a quick recasting of the momentum $k(E) = \sqrt{E}$

$$W(\omega_{is}) \propto \int \sqrt{E}\sqrt{E+\varepsilon}\rho_e(E)\rho_h(E+\varepsilon)e^{-\left|\frac{\varepsilon}{\Delta}\right|} dE. \quad 1.7.11$$

The energy root terms can be ignored as they are dwarfed by the exponential term. Additionally, the density of states expressions can be replaced by the Fermi-Dirac filling factors $f(E)$ to yield, finally,

$$W(\omega_{is}) \propto \int f(E)\big(1 - f(E+\varepsilon)\big)e^{-|\varepsilon/\Delta|}\, dE. \qquad 1.7.12$$

The simple expression given in Eqn. 1.7.12 can be used to reproduce the responses from a variety of samples, excitation energies, and geometries (note that no geometric considerations were invoked here – this treatment relied only on the behavior of a metallic charge density at an interface).

CHAPTER 2: Orientation-Dependent Handedness of Chiral Plasmons

2.1: Raman Optical Activity: Chirality and Handedness

2.1.1: Definitions

Raman optical activity (ROA) refers to the differential *scattering* of chiral molecules under right (RCP) and left (LCP) circularly polarized light [51]. This is distinguished from the optical activity presented herein, which while still within the framework of Raman scattering, instead is plasmonic (rather than molecular) in nature. Dichroism is the differential *absorption* of polarized components of the incident light [10]. The proceeding sections will deal with differential scattering of both linearly polarized light (LPL), and circularly polarized light (CPL). While these are strictly linear and circular ROA, since they involve real resonances where Raman consist of absorption and re-radiation, they will interchangeably be referred to as linear dichroism (LD) and circular dichroism (CD), respectively. Both effects arise from chirality of the light-matter interaction. The definition of chiral in the framework of these experiments refers to broken reflection symmetry; handedness refers to the polarization of light the sample preferentially scatters. The extent of dichroism is calculated by taking the difference in scattered intensity between spectra collected under +45°/-45° polarized light for LD, and RCP/LCP for CD. Typically, this this value is exceedingly small for molecules – on the order of parts per thousand [10]. It is attributed to cross terms in the multipolar polarizability tensor of the scatterer [52]. Though the dichroism presented here originates from plasmonic optical activity, it will be shown that it can be treated in

entirely the same way – namely, by careful formulation of the sample polarizability tensor.

2.1.2: Chiral connectedness

The definition of chirality in terms of non-superimposable mirror images, since based on a discrete transformation, leads to difficulty when attempts are made to quantify the extent of chirality. These considerations are exacerbated by the paradox of chiral connectedness. Based on its historical definition a mirror symmetric object should have a chirality of zero. For a non-mirror-symmetric object, its two enantiomers should be of opposite sign so that the sign of one exactly flips upon reflection into the other. In practice, however, any continuous object may be taken continuously from one enantiomer to the other without ever passing through a state of zero chirality. These considerations constitute the paradox of chiral connectedness, and for many years hampered efforts into the quantification of chirality.

A rigorous mathematical definition for the quantification of chirality and handedness was given by Efrati and Irvine [53]. In this work, the authors construct the handedness of an object such that it depends on the direction from which the object is viewed. In this way, an object can be considered left or right handed depending on how it is oriented in the plane parallel to excitation. By incorporating this orientation-dependence into the object's handedness tensor, chiral connectedness is now fully accounted for: this treatment allows for objects that both lack mirror symmetry/have no net chirality and have mirror symmetry/have net chirality. The orientation-dependent

handedness of chiral plasmons, which will be explored in this chapter, allows a direct investigation of these principles.

2.1.3: Two- and three-dimensional chirality

One last statement to be made regarding chiral response is the distinction between two- and three-dimensional chirality. Three-dimensional (bulk) chirality is defined by the lack of any mirror symmetry in a continuous object – no matter how the object is rotated in 3D space, it can never be brought into congruence with its mirror image. Two-dimensional (planar chirality) is an object that maintains its chirality in two-dimensions only – in other words, it can be brought into agreement with its enantiomer if it is lifted out of the plane.

The disparate nature of 2- and 3-D chirality manifests in markedly different optical responses. For one, any object with bulk chirality obeys the Lorentz reciprocity theorem, in that it maintains its handedness even when the direction of excitation is reversed ($\vec{k} \rightarrow -\vec{k}$). In contrast, planar chiral objects are not governed by Lorentz reciprocity and reverse their handedness upon light path reversal. According to previous analysis [54], plasmonic nanostructures are capable of sustaining both bulk and planar chiral response. Furthermore, the two are readily disentangled by a straightforward decomposition of the scattering matrix into its symmetric and anti-symmetric components. More details on the nature of the scattering matrix are given in the next section. In general, though, any square matrix M can be decomposed into its symmetric (s) and anti-symmetric (as) components through use of the matrix transpose, M^T, as:

$$M = M_s + M_{as} = \frac{M+M^T}{2} + \frac{M-M^T}{2}. \qquad 2.1.1$$

The anti-symmetric component follows Lorentz reciprocity and is therefore responsible for the 3D chiral response. For the symmetric component,

$$M_s = \begin{pmatrix} A & B \\ C & D \end{pmatrix}, \qquad 2.1.2$$

any 2D chirality will be given by $Im\left[\frac{2B}{A-D}\right]$. These relations will eventually be used to disentangle the chiral response experimentally observed in the nantenna.

2.2: Framework: Multipolar Raman Scattering on Plasmons

Since the measurements are carried out in the far-field, the electric and magnetic fields are strictly transverse and therefore fully characterized by two-element spinors, which for propagation along $\hat{z}$ are:

$$\hat{\varepsilon} = \begin{pmatrix} \varepsilon_x \\ \varepsilon_y \end{pmatrix} \qquad 2.2.1a$$

$$\hat{h} = \begin{pmatrix} h_x \\ h_y \end{pmatrix} = \hat{k} \times \hat{\varepsilon} = \begin{pmatrix} -\varepsilon_y \\ \varepsilon_x \end{pmatrix} \qquad 2.2.1b$$

Since the measurements are limited to the electric field the relation between scattered and incident fields is completely determined by a 2x2 matrix, with inherent ambiguity since the electric and magnetic components are wrapped into a single 2x1 vector $\hat{\epsilon}$:

$$\hat{\epsilon} = \begin{pmatrix} \epsilon_x \\ \epsilon_y \end{pmatrix} = \begin{pmatrix} h_y \\ -h_x \end{pmatrix} \qquad 2.2.2$$

The scattering matrix that connects the incident (ϵ_i) and scattered ($\hat{\epsilon}_s$) fields is given by the wavelength-dependent polarizability tensor $\alpha(\lambda)$ of Raman scattering theory. Formally, the scattered intensity that results from this interaction is mediated by the excitation and emission potentials, V_{exc} and V_{em}, as

$$I = |V_{em} \cdot V_{exc}|^2 = |\langle \hat{\epsilon}_s | \alpha(\lambda) \, | \hat{\epsilon}_i \rangle|^2 \quad 2.2.3$$

Here, α is a complex-valued, 2x2 matrix contained in the SU(2) vector space. Because α is the culmination of an excitation-emission process, it can further be decomposed into the product of two separate 2x2 matrices which act on their respective fields:

$$I = |V_{em} \cdot V_{exc}|^2 = |\langle \hat{\epsilon}_s | \alpha(\lambda) \, | \hat{\epsilon}_i \rangle|^2 = |\langle \hat{\epsilon}_s | a_{em} \cdot a_{exc} \, | \hat{\epsilon}_i \rangle|^2 \quad 2.2.4$$

In most cases α is symmetric, such that $a_{em}^{\dagger} = a_{exc}$, and dipolar, such that

$$\alpha = a_{em}^{\dagger} \cdot a_{exc} = |a|^2 = \begin{pmatrix} d^2 & 0 \\ 0 & 0 \end{pmatrix}. \quad 2.2.5$$

It will be shown presently that neither of these assumptions hold in the case of the nanosphere dimers. Unique identification of the elements of α is done by combining measurements in circular and linear polarization bases, which allow for unambiguous determination of each active matrix element. This is enabled by the experimental design in the next section.

Meanwhile, a full description of the optical activity of the nanosphere dimers necessitates consideration of the light-matter interaction potential that mediates the Raman scattering process. For a structure with length scale comparable to the wavelength of light, the plane wave approximation of the long-wave limit breaks down and field gradients cannot be ignored. Expanding the light-matter interaction $\hat{V} \sim \vec{A} \cdot \vec{\nabla}$ to first order in spatial dispersion [9, 55]

$$\hat{V} \sim \hat{d} \cdot \hat{\epsilon} + \frac{i}{2} \zeta \left(\hat{k} \times \hat{\epsilon} \cdot \hat{m} + \hat{\epsilon} \cdot \hat{q} \cdot \hat{k} \right) \quad 2.2.6$$

where $\zeta = |kr|$ is the smallness parameter, and the terms in the parenthesis are the magnetic dipole m and electric quadrupole q terms that for $\zeta \sim 1$become comparable to the standard electric dipole d interaction. The details of this derivation are presented in

the Appendix. Although formally V involves polar axial and dyadic vectors for $\hat{z}$-propagation, it can be completely represented by the 2x2 scattering matrices α. As before [55], for a uniaxial object with multipoles d, m, and q along the dimer principal (long) axis, and for long axis along the laboratory $\hat{x}$:

$$d_x \equiv d = \begin{pmatrix} d & 0 \\ 0 & 0 \end{pmatrix},\ q_{xz} \equiv q = \begin{pmatrix} iq & 0 \\ 0 & 0 \end{pmatrix},\ m_x \equiv m = \begin{pmatrix} 0 & -im \\ 0 & 0 \end{pmatrix} \qquad 2.2.7$$

The most general interaction matrix then contains a linear combination of these three terms such that it is of the form

$$a_{dqm} = \begin{pmatrix} d + iq & -im \\ 0 & 0 \end{pmatrix}. \qquad 2.2.8$$

Presently, it will be shown that chiral response arises from the broken symmetry between excitation and re-radiation, where the excitation proceeds through all available multipolar channels (d, q, m above), and the emission is strictly dipolar (d). In this case, the α matrix becomes

$$\alpha = a_{em}^{\dagger} \cdot a_{exc} = \begin{pmatrix} d & 0 \\ 0 & 0 \end{pmatrix}\begin{pmatrix} d + iq & -im \\ 0 & 0 \end{pmatrix} = \begin{pmatrix} d(d + iq) & -imd \\ 0 & 0 \end{pmatrix}. \qquad 2.2.9$$

In the subsequent sections, it will be shown that this matrix explains both the linear and circular dichroic response of the BPE-functionalized dimers.

2.3: Linear Dichroism

Linear dichroism (LD) is investigated by continuously monitoring the SERS response of the dimers to linearly polarized light. Here, a half-wave plate (HWP) is used to rotate the polarization angle ϕ of the incident field, which is initially horizontally polarized. The backscattered Raman signal is collected through the same plate, which reverses its action. The double-pass geometry ensures the backscatter light polarized parallel to the incident field appears horizontal (h) while perpendicular scattering appears vertically polarized (v). In most measurements a polarized beam splitting cube is used to simultaneously record the spectra in these two orthogonal polarization channels. The signal is dispersed onto a CCD array using a 0.5-m monochromator (Shamrock 500i, Andor). A microscope objective with NA=0.65 is used to record spectra on individual dimers, which are rotated such that they are horizontal (parallel to initial polarization). The overall polarization extinction of the optical train is >100:1. See Fig. 2.3.1 for details.

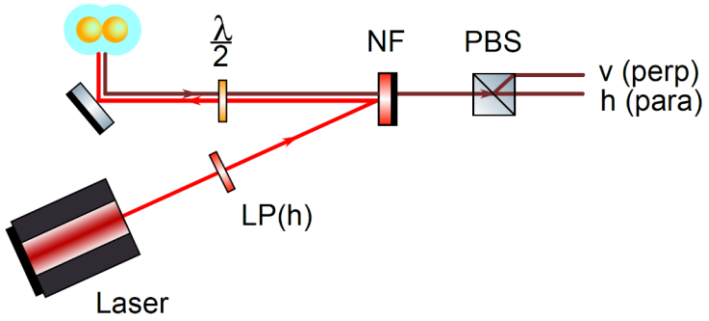

Figure 2.3.1. Experimental design for the linear dichroism experiments. Linearly polarized light from a continuous wave laser source first passes through a linear polarizer (LP) so that it is oriented along the horizontal. The light is then incident on a notch filter (NF) centered at the laser wavelength which acts as a mirror. The light then passes through a halfwave plate (HWP) at angle φ which rotates the light by angle 2φ. After interaction with a single dimer, the

backscattered Raman signal passes back through the HWP, which effectively reverses the original rotation, and through the NF onto a polarizing beam splitter (PBS). The PBS decomposed the signal into components parallel (h) and perpendicular (v) to the original polarization (h).

An example of a complete LD measurement in shown in Fig. 2.3.2 for dimer D1. It consists of recording complete spectra at incident polarization angles ϕ between 0° and 360° with 2° intervals, over the course of 2 hours total acquisition time. We consider the background-subtracted molecular lines as well as the two characteristic spectral components highlighted in Fig. 2.3.2: the blue wing of the continuum, integrated between Raman shifts of 1900 cm^{-1} and 2100 cm^{-1}, and the red wing of the continuum, integrated between 350 cm^{-1} and 550 cm^{-1}. The color-coded polar plots of these segments are presented in Fig. 2.3.2f-k. In all such plots, ϕ =0° corresponds to incident polarization aligned with the long axis of the dimer. To the extent that the graphs maintain reflection symmetry about both x- and y-axes, the response is classified as achiral. The small asymmetric deviations of the data from the fits can be taken as chirality in response that is practically ignorable.

In addition to a small, wavelength-dependent isotropic term that persists across much of the spectrum ($c(\lambda)$), the red and blue wings of the continuum contain unique scattering terms which can be readily deconstructed. The blue wing is strictly dipolar, with polarization matrix given by Eqn. 2.2.5 and scattering intensity

$$\begin{bmatrix} I_{\parallel}(\phi) \\ I_{\perp}(\phi) \end{bmatrix} = d^4 \begin{bmatrix} \cos\phi^4 \\ \sin\phi^2 \cos\phi^2 \end{bmatrix} \equiv I_d(\phi). \qquad 2.3.1$$

The red wing of the continuum of an individual dimer displays an additional, transverse feature along the dimer short axis (φ=90°, Fig. 2.3.2 (j)) in the parallel channel, with no new features materializing in the perpendicular channel. These two observations are sufficient to uniquely assign this component as strictly magnetic scattering, with polarizability

$$\alpha_m = M^2 \begin{pmatrix} i & 0 \\ 0 & -i \end{pmatrix} \quad \text{2.3.2a}$$

and observable scattering intensity

$$\begin{bmatrix} I_{\parallel}(\phi) \\ I_{\perp}(\phi) \end{bmatrix} = M^4 \begin{bmatrix} (\cos\phi^2 - \sin\phi^2)^2 \\ 4\sin\phi^2\cos\phi^2 \end{bmatrix} \equiv I_M(\phi). \quad \text{2.3.2b}$$

While the perpendicular channel response retains the same characteristic symmetric four-lobe pattern along the ±45° axes as in the dipolar scattering of Eqn. 2.3.1, the parallel channel contains both long (φ=0°) and short (φ=90°) axis response. No mixing is observed between this channel and the dipolar response given by I_d, which is assured by adding the sum of the two independent channels together. The total intensity of the three overlapping bands can be expressed and fit to:

$$\begin{bmatrix} I_{\parallel}(\phi) \\ I_{\perp}(\phi) \end{bmatrix} = a(\lambda)I_d(\phi) + b(\lambda)I_M(\phi) + c(\lambda) \quad \text{2.3.3}$$

where a, b, and c are the wavelength-dependent coefficients that weight the respective terms. The relative contributions of each of these three components vary from dimer to dimer, but the overall picture does not change. Remarkably, the Raman spectrum of the magnetic component M, which is isolated at φ=90° in the parallel channel, does not contain any molecular lines. Instead, the molecular SERS is entirely excited and broadcast through the dipolar plasmon.

In all cases, the polarization of the molecular lines exactly follows that of the blue continuum. Due to the higher signal-to-noise afforded by the molecular signature, as well as its faithful reporting on the metal polarization, all subsequent polar plots will be integrated under the strongest vibrational peak (1640 cm^{-1}) unless otherwise indicated.

Fig. 2.3.3 shows the angular plots of the polarized SERS from three different dimers, D1, D2 and D3. While dimer D1 appears achiral, the reflection symmetry in the perpendicular channel is broken for dimers D2 and D3. They both show linear dichroism with opposite handedness: the scattering intensity is larger at +45° for D2, while D3 shows largest response along -45°. The observed LD is readily reproduced by using the polarizability matrix in Eqn. 2.2.9, which incorporates the electric quadrupole and magnetic dipole terms in addition to the previous electric dipole:

$$I_{LD} = \begin{bmatrix} I_{\parallel}(\phi) \\ I_{\perp}(\phi) \end{bmatrix} = d^2[d^2 \cos\phi^2 + \ |q\cos\phi + m\sin\phi|^2\ ] \begin{bmatrix} \cos\phi^2 \\ \sin\phi^2 \end{bmatrix} \qquad 2.3.4$$

Full spectral decomposition is now possible by the weighted sum

$$I(\lambda, \varphi) = a(\lambda) I_{LD}(\varphi) + b(\lambda) I_M(\varphi) + c(\lambda) \qquad 2.3.5$$

where the previous special case of achiral dipolar scattering I_d has been replaced with the asymmetric $\{d, m, q\}$ response of linear dichroism, I_{LD}. The color-coded spectrum of Fig. 2.3.2 clarifies that all molecular lines follow the same chiral response – the molecule couples to the far-field via the chiral plasmon of the dimer. The resonance, which was apparently dipolar on D1, is now chiral on D2 and D3. The additional magnetic band assignment does not change.

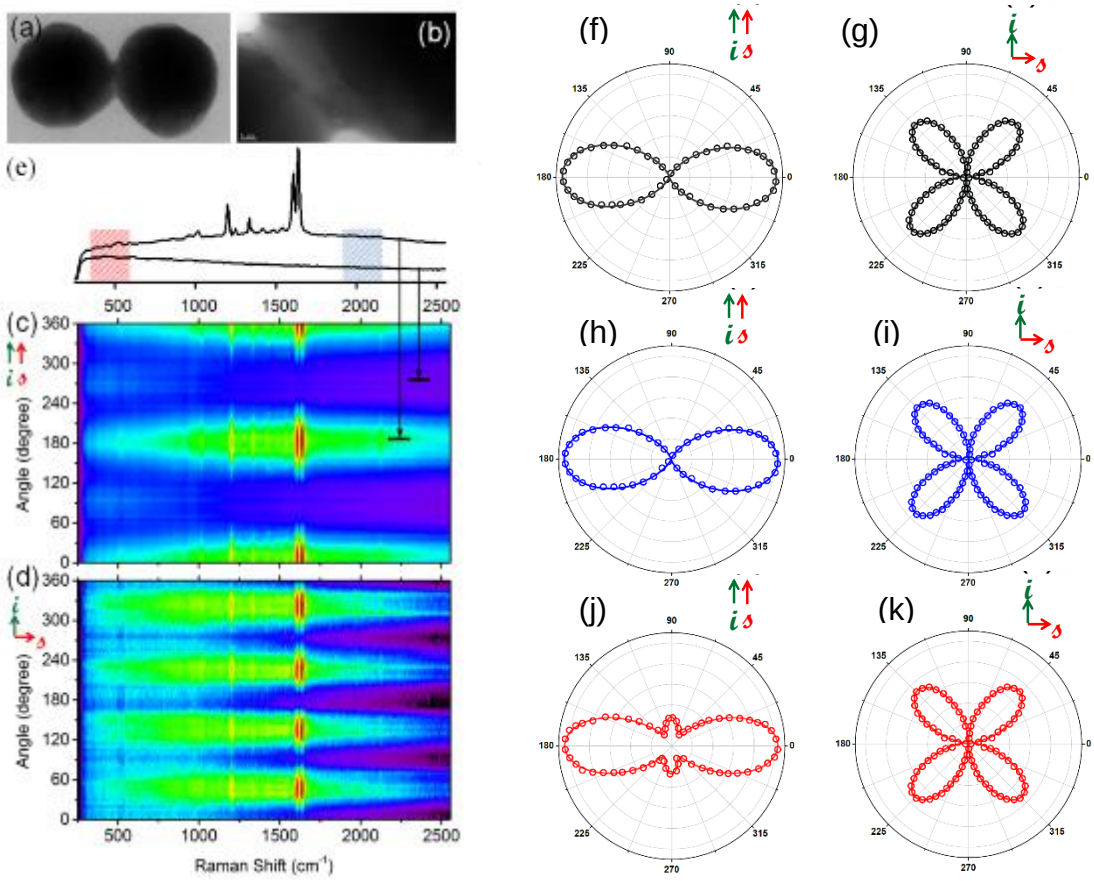

Figure 2.3.2. (a) Transmission electron micrograph image of an isolated dimer formed by two relatively spherical dimers. (b) Prolonged exposure (either to optical or electron beams) reveals a fusing of the two spheres. Plots (c) and (d) show the Raman spectra as a function of time recorded for the linear experiment in the parallel and perpendicular channels, respectively, while a representative spectrum is shown in (e). Several spectral slices are presented here, and the color-coded wings represent the quadrupolar (red) and dipolar (blue) wings of the continuum. Polar plots are presented for the most intense vibrational line, 1640 cm^{-1} (f, g), the blue continuum (h, i), and the red continuum (j, k) in the parallel (left column) and perpendicular (right

column) channels. The molecular lines strictly follow the polarization of the dipolar (blue) wing in every case, and do not impart any distinct signature of their own.

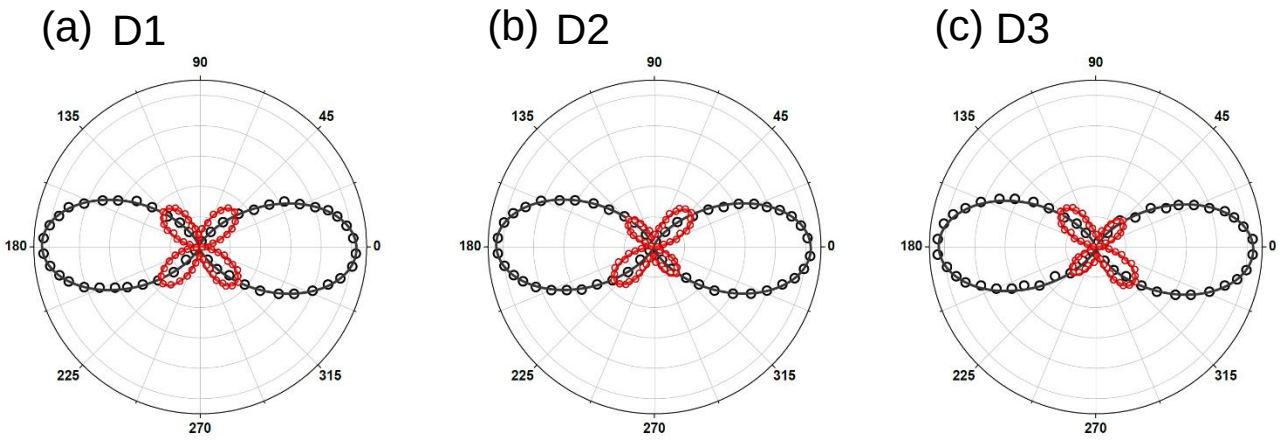

Fig. 2.3.3. The results of the linear experiment are presented here for three dimers: D1, of Fig. 2.3.2, as well as two new particles: D2 and D3. (a) While D1 showed clear reflection symmetry in its perpendicular channel response (red trace), (b) D2 and (c) D3 show a broken symmetry that favors either +45° or -45° in their perpendicular channel response (red traces). This effect constitutes linear dichroism.

2.4: Circular Dichroism

Circular dichroism (CD) is investigated by continuously monitoring the SERS intensity of the dimers under excitation in a circularly polarized basis. Here, a quarter-wave plate (QWP) at angle φ induces a phase shift of $e^{i2\varphi}$ between x- and y-components of the field [56]. As the QWP is rotated, the polarization changes continuously from horizontal (φ=0°), to right circularly polarized (RCP, φ=45°), back to horizontal (φ=90°), and to left circularly polarized (LCP, φ=135°). The QWP is rotated through a full 360° and the Raman response is recorded every 2°. The polarization states generated as a function of this rotation are shown in Fig. 2.4.1.

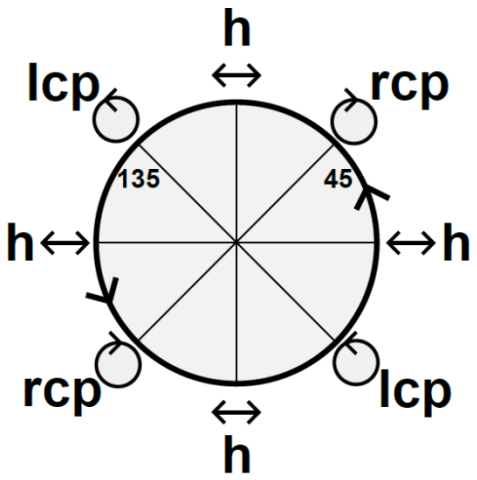

Figure 2.4.1. Polarization states generated as a function of the angle the fast axis of the quarterwave plate makes with the original linear polarization, φ. When the two are aligned (φ=0°, 90°, 180°, 270°) the polarization is unchanged. φ=45°,225° generates RCP, while φ=135°,315° generates LCP. At intermediate angles elliptical polarization is generated, with the handedness defined by the CP of that quadrant.

The experimental geometry is shown in Fig. 2.4.2. There are a few differences between the experimental design for the QWP measurements here and the HWP measurements of Fig. 2.3.1. First, the QWP is placed in single (rather than double) pass geometry. Additionally, due to the complex (and constantly evolving) state of the light, the signal is not decomposed into orthogonal channels – the total scattering intensity is recorded instead.

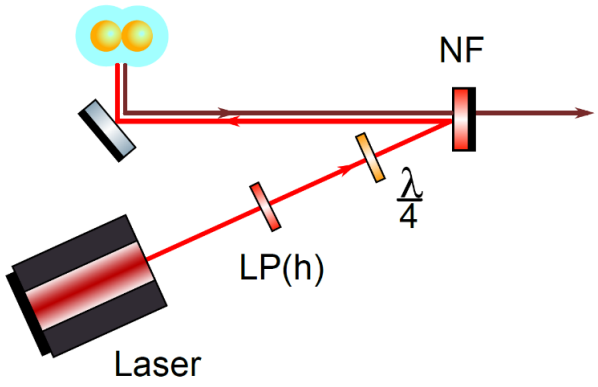

Figure 2.4.2. Experimental design for the circular dichroism experiments. Linearly polarized light from a continuous wave laser source first passes through a linear polarizer (LP) so that it is oriented along the horizontal. The light is then directed towards a quarterwave plate (QWP, λ/4) at angle φ which induces phase shift $e^{i2\varphi}$ between the x- and y-components of the field. After interaction with a single dimer, the backscattered Raman passes through a notch filter (NF) centered at the Rayleigh wavelength, and the full, open-channel signal is recorded.

An example of a complete CD measurement is shown in Fig. 2.4.3. Here, the dimer is oriented horizontally such that it is aligned with the initial horizontal polarization generated at $\varphi = \{0°, 90°, 180°, 270°\}$, which accounts for the large response at these points. Intermediate angles of $\varphi = \{45°, 135°\}$ report on the handedness of the dimer. Evidently, the dimer presented in Fig. 2.4.3 is left-handed based on its increased

response at $\varphi = 135°$. It should be repeated here that, while the polar plots are typically constructed by integrating under the molecular line, it is the plasmonic dichroism that is being observed here. In every case for the CD experiments, in analogy with the LD results of Fig. 2.3.2, the molecular lines exactly follow the polarization of the antenna on which they reside and as such, the response is strictly that of the nantenna.

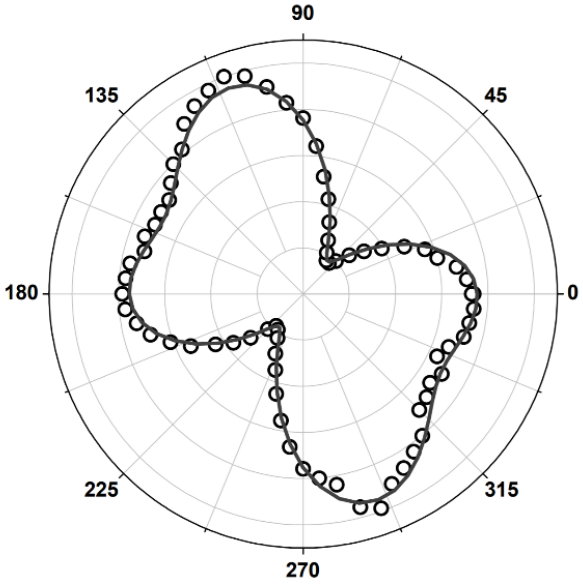

Figure 2.4.3. A complete circular dichroism (CD) measurement performed on a single dimer (D3 from Fig. 2.3.3) showing its continuous response as function of the QWP angle, φ. As the dimer is oriented horizontally, the increased response along $\varphi = \{0°, 90°, 180°, 270°\}$ is due to alignment of the dimer long axis with the linear polarization generated at these angles. The differential scattering along $\varphi = \pm 45°$ instead reports on the handedness of the antenna. Here, preferential response along $\varphi = -45$, which corresponds to LCP, indicates that the dimer is a LH object.

The response is fully reproducible using the same multipolar α matrix of Eqn. 2.2.9. While the cross-term between q and m was responsible for the extent of LD, CD

is dictated by the cross term between d and m. Consequently, as the two dichroisms are controlled by entirely different terms, the linear and circular experiments as performed on a single dimer can be joint-fit to a set of shared $\{d, q, m\}$ parameters.

Both the sign and magnitude of the handedness observed is entirely dimer dependent. In fact, repeated measurements on dozens of dimers reveal that the handedness is almost perfectly evenly split between left- and right-handed response. The magnitude of the CD, as defined by the differential intensity of the scattering under RCP and LCP,

$$CD = \frac{I_{RCP} - I_{LCP}}{I_{RCP} + I_{LCP}}$$

is found to be as large as $CD = |0.6|$ in some cases. Such a pronounced response (~parts per ten) is orders of magnitude larger than the CD typically observed in molecules (~parts per thousand). This is the first inclination that plasmonic handedness is surprisingly distinct from the more familiar molecular CD.

2.5: Orientation-Dependent Handedness

In addition to the markedly stronger extent of CD observed in plasmons, they also display an entirely unique in-plane orientation-dependent handedness (ODH). Though this ODH is apparent in both CD and LD, its appearance in CD will be of particular interest here. Indeed, the ODH that manifests in the LD experiments is rather straightforward and expected in uniaxial objects such as the nanoscale dimers. The CD, though counterintuitive, has important implications which will be explored in detail here.

2.5.1 Orientation-dependent linear handedness

In-plane orientation dependence in the LD signal is easy to rationalize: as the long axis of the dimer controls the direction of the radiation, the observed polarization pattern is expected to rotate with the nantenna. This is illustrated in Fig. 2.5.1, whereby a 90° rotation of the sample in the plane perpendicular to the direction of excitation rotates the parallel and perpendicular channel response by the same 90°. While apparently straightforward, this rotation has the effect of inverting the linear handedness – while this dimer showed preferential response along the -45° in the perpendicular channel originally, after the rotation it now scatters more strongly along +45°. Mathematically, this effect can be achieved by simply rotating the polarizability matrix (originally α_{+45}) using the 2D rotation matrix $R_\varphi = \begin{pmatrix} \cos\varphi & -\sin\varphi \\ \sin\varphi & \cos\varphi \end{pmatrix}$:

$$\alpha_{-45} = R_{\pi/2}^{T} \cdot \alpha_{+45} \cdot R_{\pi/2} \qquad 2.5.1$$

which effectively flips the sign of the linear dichroism term, mq, from (+) to (-).

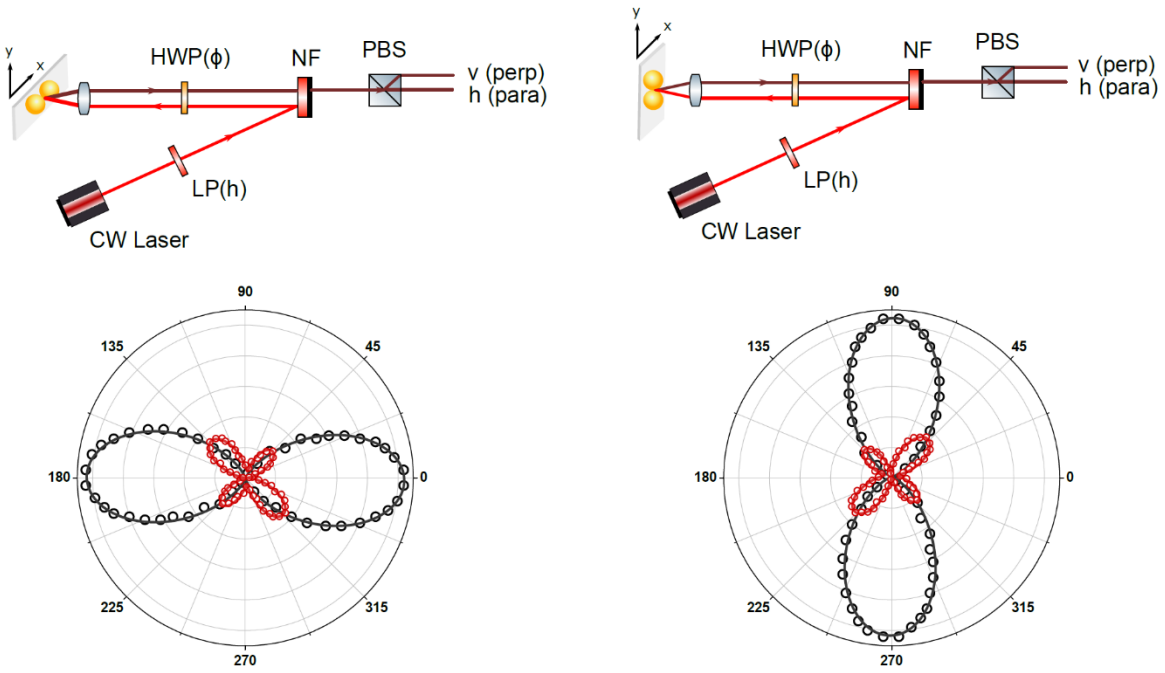

Figure 2.5.1. Observed orientation-dependent handedness in the linear dichroism (LD) experiments. As the direction of the scattered signal follows the dimer long (inter-particle) axis, any in-plane rotation φ of the sample cause a corresponding rotation of the polar plots by the same angle φ. Though intuitive, such a rotation as that shown here (φ=90°) has the important effect of directly inverting the linear handedness.

2.5.2 Orientation-dependent circular handedness

Less intuitive is that this effect of 90°-ODH is mirrored in the circular experiments. Here, the same 90° rotation *in the plane perpendicular to excitation* effectively takes the same dimer from a LH to RH scatterer. This is shown explicitly in Fig. 2.5.2

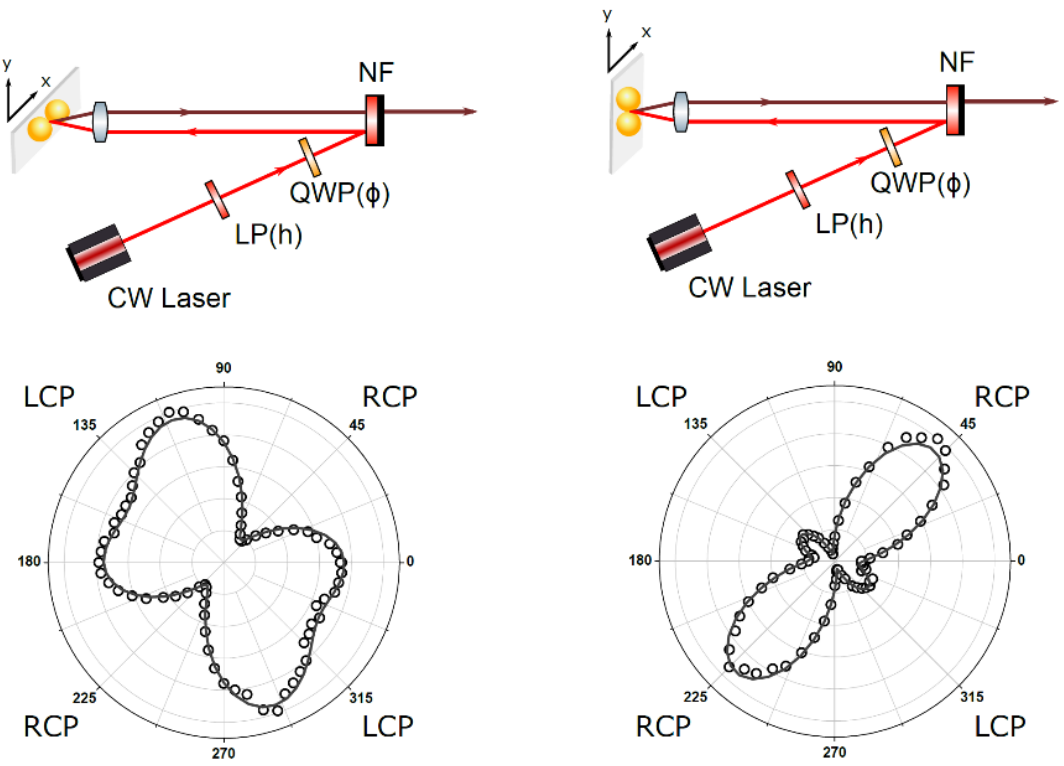

Figure 2.5.2. Observed orientation-dependent handedness in the circular dichroism (CD) experiments. Here, a 90° in-plane rotation of the sample effectively takes the dimer (D3) from a left-handed (LH) to right-handed (RH) scatterer.

This effect is so counterintuitive based on the very definition of chirality, whereby a mirror reflection is strictly necessary to transform a chiral body from one enantiomer to its other in three dimensions. That a simple in-plane rotation can transform handedness in such a way is indicative of a higher order transformation. To see this, consider the case of a two-dimensional chiral body, such as a flat “L” written on a piece of paper. To transform the “L” from it’s left-handed (native) enantiomer into its mirror image, it can simply be lifted off the page and rotated around a 180° arc. While this transformation is occurring continuously in three dimensions, it looks strange when projected onto the

two-dimensional plane of the original page. Indeed, to a two-dimensional observer, there seems to be no way that such a continuous action should be possible.

To understand what type of “hidden” transformation is occurring, consider the sample matrices required to reproduce the LH and RH scattering response. The handedness is dictated by the sign of the CD term, md. For a horizontally-oriented particle, the RH response is given by (letting $q = 0$ as it does not directly factor in to the CD):

$$\alpha_{x,RH} = \begin{pmatrix} d^2 & imd \\ 0 & 0 \end{pmatrix}. \tag{2.5.2}$$

If this matrix is rotated by 90° using standard 2D rotation matrix $R_{\pi/2}$, the resulting matrix, which is now oriented vertically, is still RH – that is, the standard in-plane rotation, which is what is presumably being enacted in the lab, is not sufficient to described the observed ODH which transforms $\alpha_{x,RH}$ into $\alpha_{y,LH}$:

$$\alpha_{y,LH} \neq R_{\pi/2}^{T} \cdot \alpha_{x,RH} \cdot R_{\pi/2} = \alpha_{y,RH}. \tag{2.5.3}$$

In order for the RH matrix $\alpha_{x,RH}$ to be transformed into its LH enantiomer, the matrix must undergo a *complex conjugation* in addition to the standard 90° rotation. In analogy with Eqn. 2.5.3, the requisite transition is instead

$$\alpha_{y,LH} = \left(R_{\pi/2}^{T} \cdot \alpha_{x,RH} \cdot R_{\pi/2}\right)^{*}. \tag{2.5.4}$$

These transformations are illustrated in Fig. 2.5.4.

The necessary complex conjugation that accompanies the solid body rotation is immediately indicative of a particular type of symmetry – namely, that of time reversal. In order for the dimer to remain invariant upon the coordinate transformation, it appears that time must simultaneously be inverted [57]. This signals that the response is PT

(parity-time) invariant, which can be understood by considering the microscopic (and hence, quantum mechanical) origins of CD.

The CD response can be reduced, as was done in Eqn. 2.5.2, into a pair of colinear polar (electric dipole) and axial (magnetic dipole) vectors. The pair is readily identified as PT-invariant if it is first recognized that parallel d and m described a RH helix ($\psi(R)$) and anti-parallel d and m describe a LH helix ($\psi(L)$). Under the parity operator $\hat{P}$, d is odd and m even such that $\hat{P}\big(\psi(R)\big) = \psi(L)$ (Fig. 2.5.4). Under time reversal $\hat{T}$, it is now d that is even and m that is odd; similarly, $\hat{T}\big(\psi(R)\big) = \psi(L)$. In total, the combination of parity and time reversal gives $\hat{T}\big[\hat{P}\big(\psi(R)\big)\big] = -\psi(R)$. In this way, the complex conjugation is identified as the time reversal under the rotation, necessary to conserve PT invariance of the dimer.

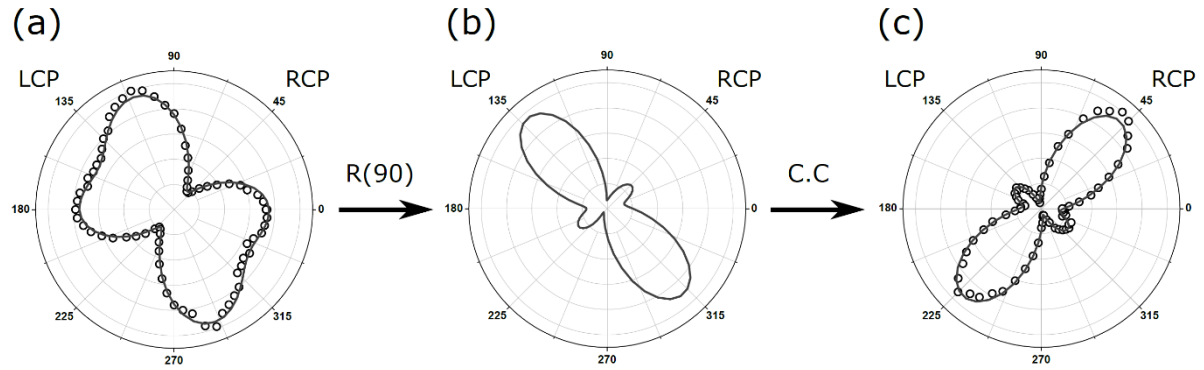

Figure 2.5.3. (a) Results of the circular dichroism experiment for dimer D3 at its original, horizontal orientation, where its scattering is preferentially left-handed. (b) Predicted response of D3 after 90° physical rotation of the sample (R(90)), which re-orients it along the vertical but retains the original LH response. (c) Actual response of the 90° in-plane rotation, which in addition to orienting the particle along the vertical, also inverts its handedness to RH response.

This can only be achieved by a subsequent complex conjugation (C.C.) of the sample scattering matrix.

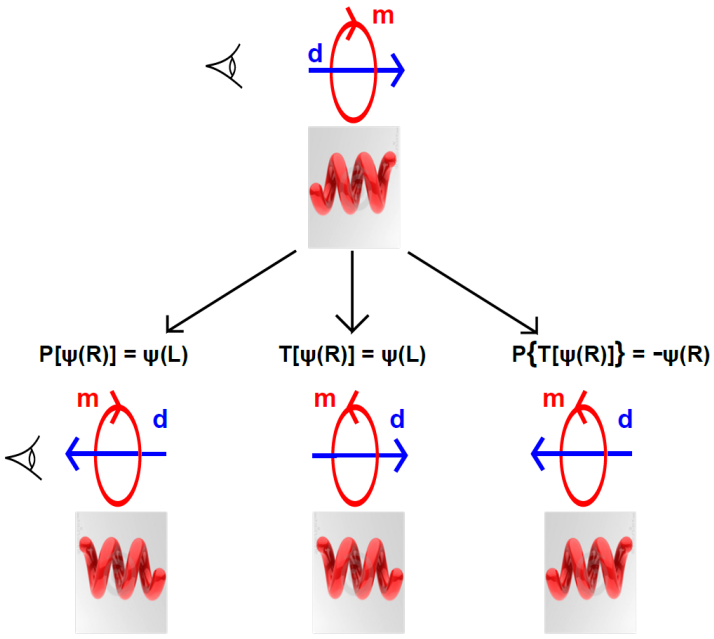

Figure 2.5.4. The effects of the parity and time operators on a system consisting of a pair of colinear electric and magnetic dipoles. A stationary observer sees a right-handed (R) helix from the combined effect of an electric dipole along $\hat{x}$ and clockwise-moving magnetic dipole. Under the parity operator P, which inverts all spatial coordinates, the electric dipole is now along $-\hat{x}$ while the magnetic dipole maintains its clockwise sense of rotation. From the same observation point, this construction now gives rise to a left-handed helix (L). The time reversal operation T, which takes all i into $-i$, is treated similarly, noting that while the electric dipole maintains its orientation along $\hat{x}$, the magnetic dipole is inverted to a counter-clockwise rotation. The combined effects of a PT operation, then, is to leave the original handedness unchanged.

2.6: Statistics and Origins of Chirality

The Raman optical activity of a large number (>50) of dimers have been mapped out fully, both at 532 nm and 633 nm excitation, with linear and circularly polarized light. A summary of the joint linear and circular results is given in Fig. 2.6.1, in the form of a scatter plot of ζ_m vs. ζ_q. Every entry in the scatter plot corresponds to a fitted parameter pair ($\zeta_m = m/d$ and $\zeta_q = q/d$) that simultaneously reproduces both the linear and circular measurements at the respective excitation colors (green for 532 nm and red for 633 nm). The pairs of measurements on any individual dimer are connected with solid lines in order to highlight the color dependence of the multipoles of a dimer. All dimers show chiral response to a different degree – indeed, achiral is a singularity that is rare in measurements on nanostructures using light of comparable wavelength.

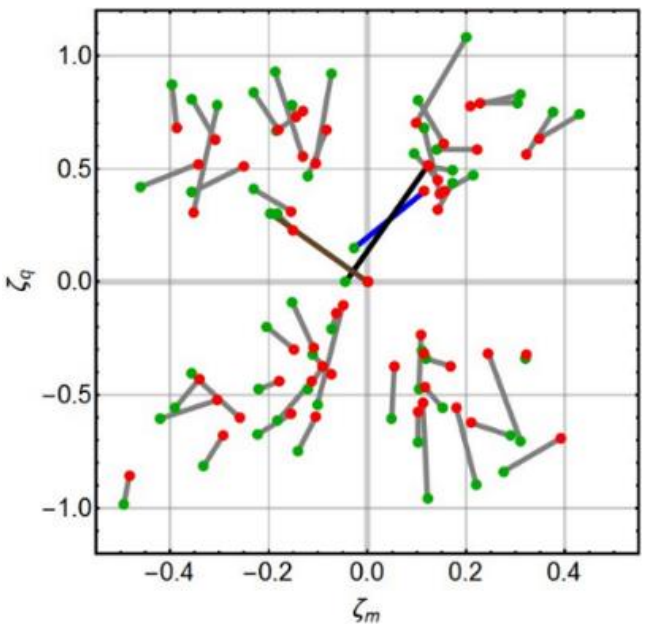

Figure 2.6.1. A brief statistical representation of the extracted fitting parameters (ζ_m, ζ_q) for ~60 dimers. In $\zeta_m - \zeta_q$ space, circular dichroism (CD=$\langle md \rangle$) and linear dichroism (LD=$\langle mq \rangle$) are easily visualized. The scatter plot contains (ζ_m, ζ_q) values obtained from join linear and circular measurements at corresponding excitation color (green for 563 nm and red for 633 nm). Measurements on a single dimer are connected by solid lines.

Clearly there is a structural origin to the observed giant chiral response and ODH. This has been explored through rigorous COMSOL simulations [58] which have identified the nanojunction itself as the origin. Using explicit simulations for the Rayleigh response on dimers, no effects arise from deviations from sphericity in the global shape of the nanospheres. It is only when the junction contact is shifted from the symmetry axis of the dimer that optical activity in analogy with the linear experiments appears (Fig. 2.6.2).

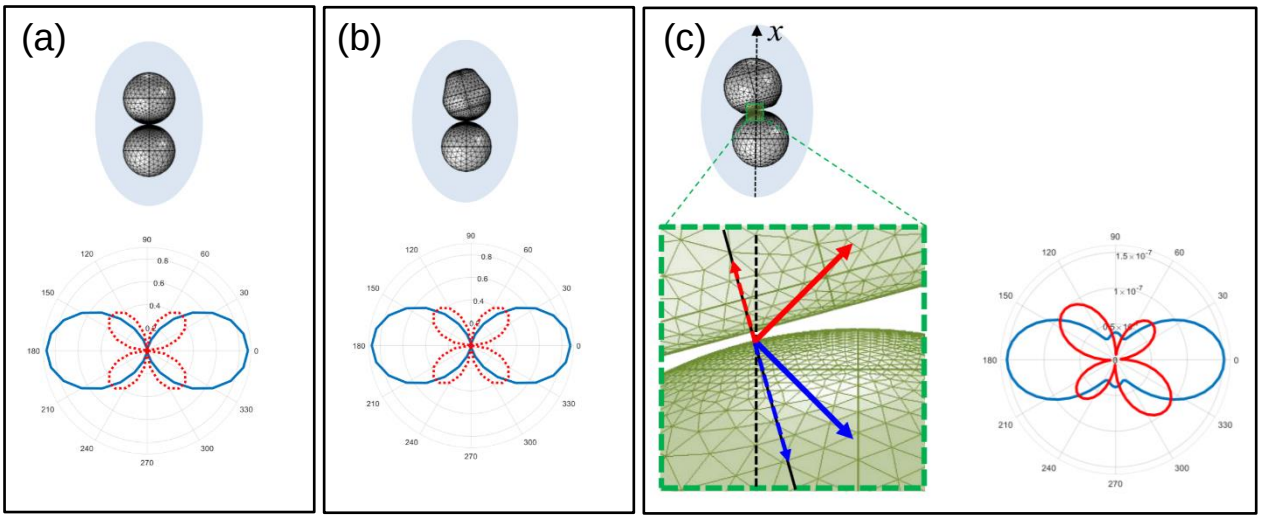

Figure 2.6.2. Results of simulations performed in COMSOL showing the linear dichroism generated in the parallel (blue) and perpendicular (red) channel for a variety of nanodimer geometries. When the dimers are entirely symmetric (a) or contain a symmetric junction, regardless of the global symmetry (b), no dichroism is observed. It is only when the axis of the junction is shifted from the interparticle axis (c) that the requisite asymmetry is generated along the ±45° line in the perpendicular channel. Reprinted with permission from [58].

The junction, then, controls the bulk of the chirality of the response: while its vorticity dictates the observed chirality, the natural impedance matching is established

with the nm-scale interparticle hot-spot, which allows for the appearance of molecular SERS. This has important implications in the recent experiments in using plasmonic nanojunctions to assess molecular chirality – the results shown here indicate that the response of the nantenna itself cannot be ignored and must be fully understood before any conclusions regarding the state of the molecule can be drawn.

2.7: Analysis of Plasmon Interaction Matrix

2.7.1 Excitation-emission asymmetry

As has been established in the preceding sections, the interaction matrix of Eqn. 2.2.9 describes fully the response of the nantenna to any polarization of incident light. In total, the interaction is governed by the action of the excitation and emission matrices (a_{em} and a_{exc}, respectively) on the incident and scattered fields ($\hat{\epsilon}_i$ and $\hat{\epsilon}_s$):

$$I = |V_{em} \cdot V_{exc}|^2 = |\langle \hat{\epsilon}_s | \alpha(\lambda) \, | \hat{\epsilon}_i \rangle|^2 = |\langle \hat{\epsilon}_s | a_{em} \cdot a_{exc} \, | \hat{\epsilon}_i \rangle|^2. \quad 2.7.1$$

These interactions are mediated by the respective excitation and emission interaction potentials, V_{em} and V_{exc}. As presented in Eqn. 2.2.9, the only matrix construction that effectively reproduces all of the observed data is given by

$$\alpha = a_{em} \cdot a_{exc} = a_d \cdot a_{dqm} = \begin{pmatrix} d(d+iq) & -imd \\ 0 & 0 \end{pmatrix}. \quad 2.7.2$$

Such a construction highlights a very unique asymmetry in the excitation-emission process: while the plasmon can be excited through all available multipolar channels, it is only able to radiate via the electric dipole. While dimers free of LD and CD response are sufficiently described by a pure electric dipolar response ($q = m = 0$ in Eqn. 2.7.2), those demonstrating chirality are only adequately describable when all terms are active.

As previously discussed, LD explicitly requires the cross-term mq, while CD is controlled by md. The Feynman diagrams for these transitions is shown in Fig. 2.7.1.

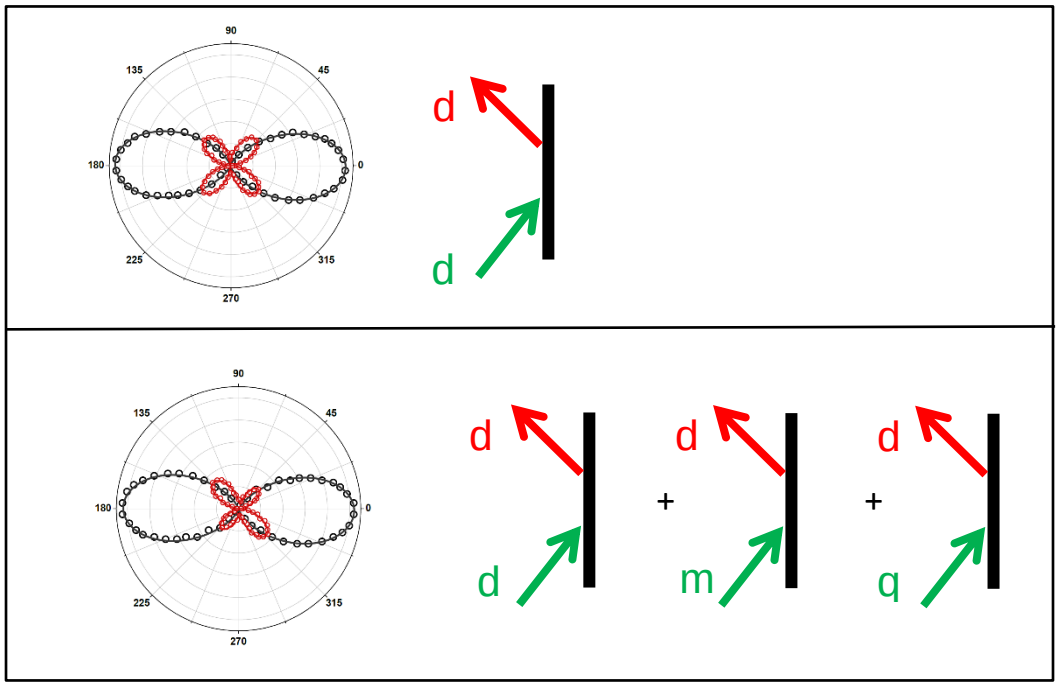

Figure 2.7.1. Top: Achiral plasmons, which lack any significant LD and CD (shown here for LD specifically), are adequately described by a pure electric dipolar transition. Bottom: For dimers which display dichroism, however, multipolar scattering channels are required in order to reproduce the observed response. In the case of LD, both m and q are necessary to explain the scattering asymmetry in the perpendicular channel (red trace).

2.7.2 Orthogonal Pauli decomposition of the interaction matrix

Recall that Raman is fourth order in the interaction process: as the measurements are made on the total intensity I, it is the square modulus of the interaction that is of interest. This further squares the polarizability matrix α, which effectively mediates the interaction as

$$|\alpha(\lambda)|^2 = |a_{em} \cdot a_{exc}|^2 = \begin{vmatrix} d(d+iq) & -imd \\ 0 & 0 \end{vmatrix}^2 \quad \text{2.7.3a}$$

$$= d^2 \begin{pmatrix} d^2+q^2 & -mq-imd \\ -mq+imd & m^2 \end{pmatrix}. \quad \text{2.7.3b}$$

In this form, the interaction matrix $|\alpha(\lambda)|^2$ is a member of the **SU(2)** vector space. In addition to serving as the foundation for the quantum mechanical treatment of two-level systems, the **SU(2)** vector space is also heavily utilized in Jones calculus of optics. Here, the incident and scattered fields are related through complex 2x2 Jones matrices. The strength of the Jones formalism lies in its direct formulation from the Maxwell equations, which retains information about the relative phases of the field components and material response. In analogy with the quantum mechanics of two-level systems, Jones vectors are confined to describing fully polarized states in the same way that wavefunctions describe coherent states.

The **SU(2)** space is completely spanned by the identity matrix σ_0 and the *optical* Pauli matrices $\{\sigma_1, \sigma_2, \sigma_3\}$, which are related to the standard spin matrices of quantum mechanics $\{\sigma_x, \sigma_y, \sigma_z\}$ as [56]

$$\sigma_0 = \begin{pmatrix} 1 & 0 \\ 0 & 1 \end{pmatrix} = I, \quad \sigma_1 = \begin{pmatrix} 1 & 0 \\ 0 & -1 \end{pmatrix} = \sigma_z, \; \sigma_2 = \begin{pmatrix} 0 & 1 \\ 1 & 0 \end{pmatrix} = \sigma_x, \quad \sigma_3 = \begin{pmatrix} 0 & -i \\ i & 0 \end{pmatrix} = \sigma_y. \quad \text{2.7.4}$$

Any complex-valued 2x2 matrix M is subsequently decomposed in the Pauli basis by:

$$M = \sum_{i=0}^{3} s_i \sigma_i = \vec{s} \cdot \vec{\sigma}$$

where $\vec{s}$ is the vector of the coefficients s_i that weight the corresponding Pauli matrices, condensed into vector notation as $\vec{\sigma} = (\sigma_0, \quad \sigma_1, \quad \sigma_2, \quad \sigma_3)^T$. For matrix $|\alpha(\lambda)|^2$, these coefficients are given by

$$s_0 = \frac{d^2}{2}(d^2 + q^2 + m^2) = N \qquad 2.7.5a$$

$$s_1 = \frac{d^2}{2}(d^2 + q^2 - m^2) = N' \qquad 2.7.5b$$

$$s_2 = -d^2\, mq \propto -mq \qquad 2.7.5c$$

$$s_3 = -d^2\, md \propto -md. \qquad 2.7.5d$$

The set of coefficients are known as the Stokes parameters and are defined by the differential intensities between horizontal (h), vertical (v), ±45°, and right/left handed circularly polarized light (RCP, LCP) [56]

$$s_0 = I_h + I_v \qquad 2.7.6a$$

$$s_1 = I_h - I_v \qquad 2.7.6b$$

$$s_2 = I_{45} - I_{-45} \qquad 2.7.6c$$

$$s_3 = I_{RCP} - I_{LCP} \qquad 2.7.6d$$

Parameter s_0 therefore describes the total intensity of the scattered light while s_1 determines the extent of horizontal/vertical anisotropy. Parameters s_2 and s_3 are of particular interest as they determine the linear and circular scattering dichroism, respectively, of the sample. For matrix $|\alpha(\lambda)|^2$, it is evident that while linear dichroism arises from the relative signs of m and q, circular dichroism is defined by the familiar cross-term of m and d.

Stokes parameters are not relegated to describing optical elements alone – any polarization state of light can also be described in terms of the differential intensities presented in Eqns. 2.7.6a-d. The set of four Stokes parameters that describe either an optical element or a polarization state is known as a Stokes vector. Transformations can be carried out directly with the Stokes vector equivalents in the Mueller calculus formalism. Now, linear transformations are represented by scalings and rotations of the four-element Stokes vector in **O(3)**. Rather than the complex 2D field vectors of Jones, Mueller calculus deals strictly with light intensities [56].

The pure polarization states of Eqn. 2.7.1 is readily recast in terms of the projection of the sample Stokes vector, $\vec{s}$, onto the polarization state $\vec{S}$:

$$|\langle\hat{\epsilon}_s|\alpha(\lambda)\,|\hat{\epsilon}_i\rangle|^2 = \langle\vec{s}|\vec{S}\rangle \qquad 2.7.8$$

The true utility of this formulation is realized when the interaction is cast on the Poincare sphere. The three orthogonal axes of the sphere are defined by the Pauli matrices $\{\sigma_1, \sigma_2, \sigma_3\} = \{\sigma_z, \sigma_x, \sigma_y\}$, with σ_0 setting the radius to unity. Based on their corresponding Pauli matrix definitions, the three axes $\sigma_1, \sigma_2, \sigma_3$ of the sphere represent the horizontal/vertical, +45°/-45°, and RCP/LCP polarization states. Stokes parameters $\{s_1, s_2, s_3\}$ give the projection of a vector (be it light or optical element) onto each axis of the sphere, thereby defining its polarization state. Using the Stokes parameters of scattering matrix $|\alpha(\lambda)|^2$ (from definitions given in Eqns. 2.7.6a-d), we can construct its normalized Stokes vector as follows.

$$\vec{s}_{|\alpha(\lambda)|^2} = \vec{s}_{\mathrm{x}} = \frac{1}{s_0}\begin{pmatrix} s_1 \\ s_2 \\ s_3 \end{pmatrix} = \frac{d^2}{N}\begin{pmatrix} (d^2+q^2-m^2)/2 \\ -mq \\ -md \end{pmatrix} = \frac{d^2}{N}\begin{pmatrix} N' \\ -mq \\ -md \end{pmatrix} \qquad 2.7.9$$

This vector is illustrated in Fig. 2.7.2, for $\{d = m = q = 1\}$. Any subsequent interactions are represented by projecting the sample vector onto the Stokes vector of the polarization state with which it interacts. For unitary transformations this corresponds simply to a rotation of the light vector, though more generally it may also be scaled by its interaction with matter.

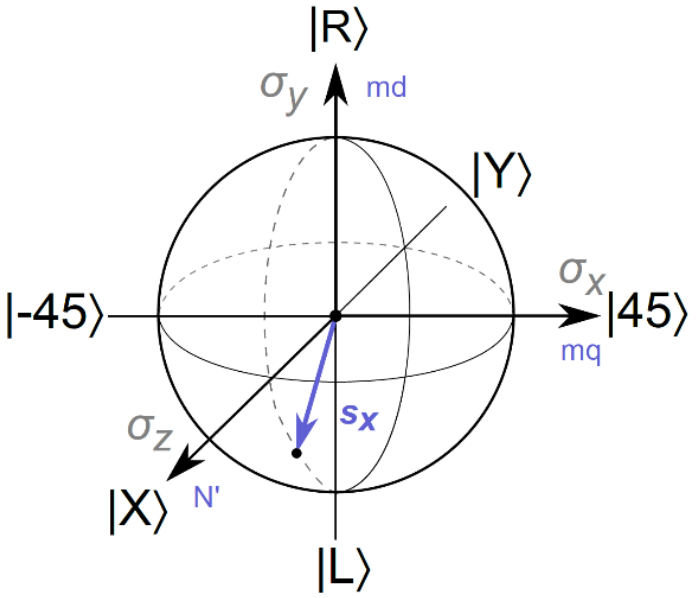

Figure 2.7.2. Representation of sample scattering vector $\vec{s}_x$ on the Poincare sphere. Sphere axes are defined by the Pauli spin matrices $\{\sigma_z, \sigma_x, \sigma_y\}$, with corresponding polarization states as indicated by the kets. The projections of the vector onto each axis are determined by the Stokes coefficients $\{s_1, s_2, s_3\}$, the forms of which are given in purple. The resultant of a light-matter interaction is determined by projecting the sample vector $\vec{s}_x$ onto the vector of the light polarization state.

The optical trains for both the LD and CD experiments can be readily constructed in both Mueller or Jones formalism. While much of the preceding analysis was confined to Jones algebra, the Stokes construction can be rapidly deployed as well. For the both

experiments, horizontally polarized light is incident on either a horizontal HWP (linear) or QWP (circular), which is subsequently rotated in angle φ, respectively. Briefly (see Appendix for details), these result in the following Stokes vectors.

$$\vec{S}_{HWP} = HWP(\varphi) \cdot h = \begin{pmatrix} 1 \\ \cos(4\varphi) \\ \sin(4\varphi) \\ 0 \end{pmatrix} \quad \text{2.7.10a}$$

$$\vec{S}_{QWP} = QWP(\chi) \cdot h = \begin{pmatrix} 1 \\ \cos(2\chi)^2 \\ \cos(2\chi)\sin(2\chi) \\ \sin(2\chi) \end{pmatrix} \quad \text{2.7.10b}$$

When cast onto the Poincare sphere, as shown in Fig. 2.7.3, the nature of the two experiments is made more apparent. The linear experiment is confined to the equator, sampling only the horizontal/vertical and +45/-45 axes as evident by the lack of any circular polarization generated here. In the circular experiment, the polarization traces out a complete figure eight as a function of φ. Starting first at the state of pure horizontal polarization, the polarization then sweeps up in a counterclockwise direction toward the RCP north pole, circles back through horizontal, subsequently down to the LCP south pole, and finally back once again to the horizontal. Note here that a single figure eight corresponds to rotation of the QWP from 0° → 180° only; a full 360° rotation simply traces this pattern twice.

Recalling that the sample scattering can be described in terms of its corresponding Stokes vector $\vec{s}$ (Fig. 2.7.2), it is immediately obvious that the interaction is 3D in nature. The linear experiment probes the projections of $\vec{s}$ in the equatorial plane: it never has projection onto the RCP/LCP axis and so the Stokes parameter s_3 is not directly accessible. To see this more clearly, project a general sample scattering

matrix $\vec{s} = (s_0 \quad s_1 \quad s_2 \quad s_3)^T$ onto both the HWP and QWP polarization states generated above:

$$\vec{s} \cdot \vec{S}_{HWP} = s_0 + s_1 \cos(4\varphi) + s_2 \sin(4\varphi) \qquad 2.7.11b$$

$$\vec{s} \cdot \vec{S}_{QWP} = s_0 + s_1 \cos(2\chi)^2 + s_2 \cos(2\chi) \sin(2\chi) + s_3 \sin(2\chi) \qquad 2.7.11b$$

While all four Stokes parameters are retained in the QWP experiment, the HWP experiment cannot access the final s_3 term of circular dichroism in a total intensity measurement. While the QWP experiment essentially samples all four Stokes parameters, it is indifferent to the sign of the LD term s_2 due to the even nature of $\cos(2\chi) \sin(2\chi)$. It is for this reason that experiments into both the linear and circular response of the dimer are crucial in order to elucidate its complete nature.

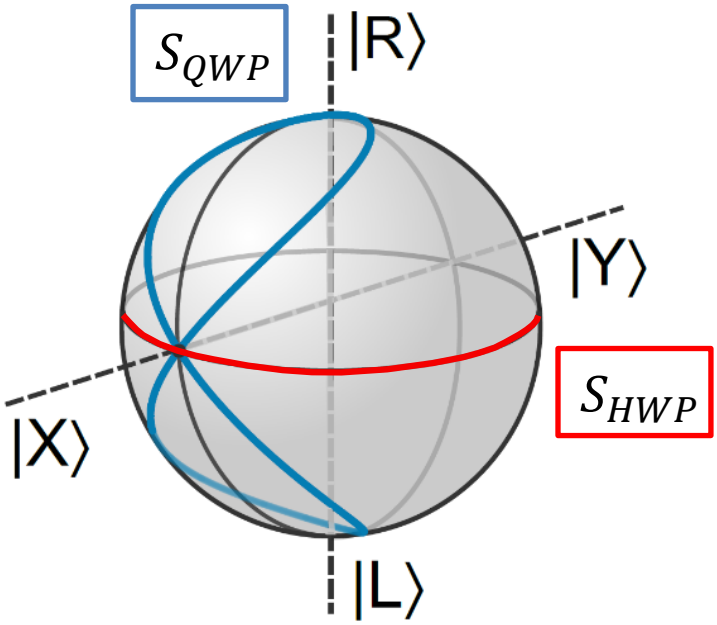

Figure. 2.7.3. The resulting paths on the Poincare sphere traced out by the linear (red) and circular (blue) experiments. While the linear experiment circles the equator of the sphere only, the circular experiment has projection onto all three of the Pauli axes, therefore accessing all of the necessary Stokes parameters.

2.7.3 Symmetric and anti-symmetric components and 2D versus 3D chirality

The distinctions between 2- and 3-D chirality, including their matrix construction and eventual optical response, were introduced in Section 2.1. For matrix $|\alpha(\lambda)|^2$ such a decomposition is particularly revealing. Taking the x-oriented particle and dropping the common d^2 term for clarity, the matrix becomes

$$|\alpha(\lambda)|^2 = \begin{pmatrix} d^2+q^2 & -mq-imd \\ -mq+imd & m^2 \end{pmatrix} \quad 2.7.12$$

and its corresponding symmetric and anti-symmetric components are as follows.

$$|\alpha(\lambda)|^2\,(s) = \begin{pmatrix} d^2+q^2 & -mq \\ -mq & m^2 \end{pmatrix} \quad 2.7.13a$$

$$|\alpha(\lambda)|^2\,(as) = \begin{pmatrix} 0 & -imd \\ +imd & 0 \end{pmatrix} \quad 2.7.13b$$

While the 3D chiral response naturally arises from the circular dichroism (with handedness given by md) of the anti-symmetric matrix, the fully real nature of the symmetric component immediately precludes any 2D chiral response.

That the chiral response is three-dimensional makes the observed circular ODH all the more peculiar – though some degree of ODH is to be expected in 2D cases, 3D responses, by their very definition, can never be brought into congruence with their enantiomer.

2.8: Extensions to Chiral Connectedness

As discussed in Section 2.1, the paradox of chiral connectedness states that any continuous object may be taken continuously from one enantiomer to the other such that the object never passes through a state of zero chirality. While this has historically been difficult (if not impossible) to realize experimentally, the ODH of the nanosphere dimers presents a unique opportunity to explore this phenomenon further. Since the optical response sustains both CD and LD, it is possible to choose Stokes trajectories that connect the optical enantiomers without passing through a wholly achiral state. Thus, identifying the chiral index of the material polarization by handedness for CD, $h = md/|m|\,|d|$ and footedness for LD, $f = mq/|m|\,|q|$, it is possible to choose trajectories such that the zero-crossings of h and f do not coincide. This can be done, for example, by rotating the initial linear polarization of light with respect to the QWP fast axis. Effectively, this action translates the figure-eight of Fig. 2.7.3 around the equator of the Poincare sphere.

Examples are shown in Fig. 2.8.1, where data recorded along continuous Stokes trajectories are mapped as LD versus CD on the $\sigma_x\sigma_y$ plane (Fig. 2.8.1c). The only trajectories that pass through the achiral origin are those that involve polarization states normal to the $\sigma_x\sigma_y$ plane, namely the $|\pm 45°\rangle$ states. Had the second component of LD also been considered, the horizontal/vertical (rather than $|\pm 45°\rangle$) differential response, the achiral state would be reached only when the Stokes vector is orthogonal to the measurement state, $\langle s|S\rangle = 0$. This cannot be avoided in 2D vector space, e.g., when measurements are limited to linear polarization and the interaction lacks projection

along σ_y. Otherwise, rather than paradoxical, chiral connectedness is the general rule: it is an exceptional trajectory that connects optical enantiomers through the achiral state.

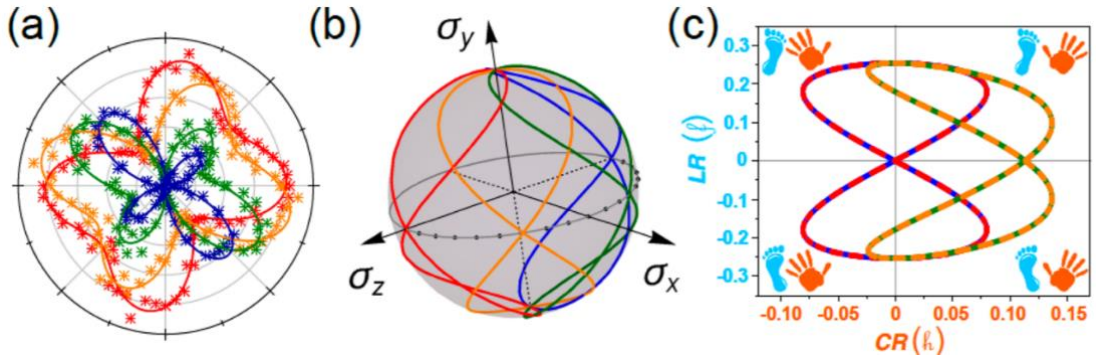

Figure 2.8.1. Chiral connectedness as illustrated in the nanosphere dimers. (a) Measured backscattered intensities as a function of rotation angle of the QWP for four initial orientations of the linear polarizer relative to the long axis of the dimer: $\varphi = 0°$ (red), $\varphi = 30°$ (orange), $\varphi = 60°$ (green), $\varphi = 90°$ (blue). (b) Color-coded trajectories of the incident Stokes vector on the Poincare sphere. (c) Projection of the measurements on the $\sigma_x\sigma_y$ plane, which corresponds to the map of footedness (LD) versus handedness (CD).

2.9: Chiral Plasmons

Ever since the introduction of the hybridization model [29], plasmonic resonances of the nanodimers are identified in analogy with diatomic molecules. Paralleling the construct of a linear combination of atomic orbitals, the $|l_1, m_1 = 0\rangle \pm |l_2, m_2 = 0\rangle$ and $|l_1, m_1 = 1\rangle \mp |l_2, m_2 = 1\rangle$ combinations of nanosphere Mie resonances are assigned to the bonding and anti-bonding dipolar and quadrupolar plasmons, with interaction energies given by the Coulomb integral of surface charge distributions. A dense

manifold of |l, ml> states cover the spectral range of the four molecular orbitals shown in Fig. 2.9.1a. The measurements described here are entirely limited to the spectral range of what is nominally considered quadrupolar states, but is here revealed to consist of additional electric and magnetic dipole (and hence, chiral) resonances. These would have been anticipated by considering the leading dipole-dipole tensor that couples plasmons on two spheres in its irreducible representation [59]. The second rank tensor leads to nine states, $D^{(1)} \otimes D^{(1)} = D^{(2)} + D^{(1)} + D^{(0)}$ which correlate with Δ +2 Π +3 Σ states of angular momentum $\Lambda = \left|m_{l,1} + m_{l,2}\right|$ = 2,1,0 along the principal quantization axis (Fig. 2.9.1b). On nanospheres, these symmetry-adapted states describe surface current: The Δ states, $|\pm 1, \pm 1\rangle$ is magnetic, with current cocirculating around the intersphere axis. The Π state, $|\pm 1,0\rangle + |0, \pm 1\rangle$ is helical, with united sphere limit $Y_{2,\pm 1} \approx (x \pm iy)z$. The three Σ states with Λ=0 come in two flavors: the binding dipolar plasmon, $|0,0\rangle$, and the vortex states, $|\pm 1, \mp 1\rangle$ that approximate magnetic monopoles. To the extent that cylindrical symmetry is maintained, $\Lambda \neq 0$ states are doubly degenerate, and the superposition of degenerate $\Lambda_{\pm}$ states leads to the Cartesian multipoles of the hybridization model (Fig. 2.9.1a). This prevails on achiral nanodimers, e.g., Fig. 2.9.1, where the excitation may be assigned to $q_{xz} \propto Y_{2,1} + Y_{2,-1}$ in the united sphere limit. Splitting of $\Lambda_{\pm}$ states is necessary to observe handed response, and the deviation of the nanosphere junction from sphericity is the origin of broken symmetry as was shown in Fig. 2.9.1. This hidden asymmetry resolves the contradiction of an achiral structure showing chiral response and at the same time exposes the true challenge of quantifying chirality.

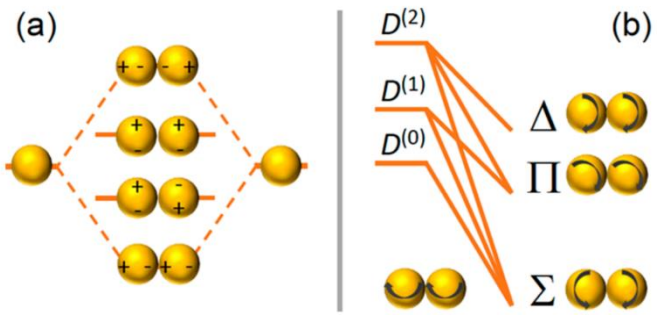

Figure 2.9.1. Plasmonic resonances. (a) The hybridization model [29] considers the interaction between Cartesian dipoles; (b) the symmetry adapted states of the dipole−dipole interaction in its irreducible spherical representation implies circulating surface current, therefore plasmons that carry angular momentum. The Δ state is the magnetic plasmon, with cocirculating current $|\pm1, \pm1\rangle$. The Π state is helical, with current that involves simultaneous circulation and translation $|\pm1, 0\rangle + |0, \pm1\rangle$ as in Figure 1. The Σ state comes in two flavors, the $|0, 0\rangle$ state equivalent to the lowest energy bonding dipolar plasmon in (a) and the counter circulating vortex states $|\pm1, \mp1\rangle$ that approximate magnetic monopoles.

CHAPTER 3: Extensions to Bi-Isotropic and Negative Index Media

3.1: Introduction: Negative Index in Linear Media

In this chapter, the multipolar terms derived in Chapter 2 will be extended and brought into congruence with familiar material parameters, such as the electric permittivity ε and magnetic permeability μ. It will be shown, rather straightforwardly, that the simultaneous excitation of d, q, m terms in the plasmonic nantenna allows for the generation of a novel type of negative index which arises from a bi-isotropic medium. Before these considerations can be discussed at length, however, a brief overview of general isotropic media, as well as the history, applications, and current strategies in negative index media (NIM) is presented.

In the case of a standard linear (reciprocal, achiral) material, the constitutive equations

$$\vec{B} = \mu\vec{H} \qquad 3.1.1a$$

$$\vec{D} = \varepsilon\vec{E} \qquad 3.1.1b$$

give rise to an index of refraction governed by [60]

$$n = \sqrt{\varepsilon\mu}. \qquad 3.1.2$$

NIM, which exhibit a negative refractive index n over some frequency range, were first proposed by Victor Veselago in 1967 [61]. In this theoretical paper, he investigates the optical properties of a then-unrealized material with simultaneously negative ε and μ (note that if only one parameter is negative, $n = \sqrt{-\varepsilon\mu} = in$ and the wave becomes entirely attenuating and therefore does not propagate). He noted a number of fascinating properties that would arise in such a medium, including a reversal of the

Doppler effect and direction of the Cherenkov radiation cone. Perhaps most important for general applications, though, was his finding that negative index generates a system in which $\{\vec{k}, \vec{E}, \vec{H}\}$ form a left-handed set. To see this, recognize that material parameter μ connects the cross-product $\vec{k} \times \vec{E}$ with the direction of the magnetic field $\vec{H}$ as follows:

$$\vec{k} \times \vec{E} \propto \mu \vec{H} \Rightarrow -\vec{H} \qquad 3.1.3$$

Here, the direction of propagation, defined by $\vec{k}$, is directed opposite to that exhibited by a normal, right-handed medium. Additionally, the Poynting vector $\vec{S}$ which defines the direction of energy flux opposes the direction of propagation in a NIM, as $\vec{S} \propto \vec{E} \times \vec{H}$. For this reason, NIM are also sometimes called “left-handed” or “backwards” media.

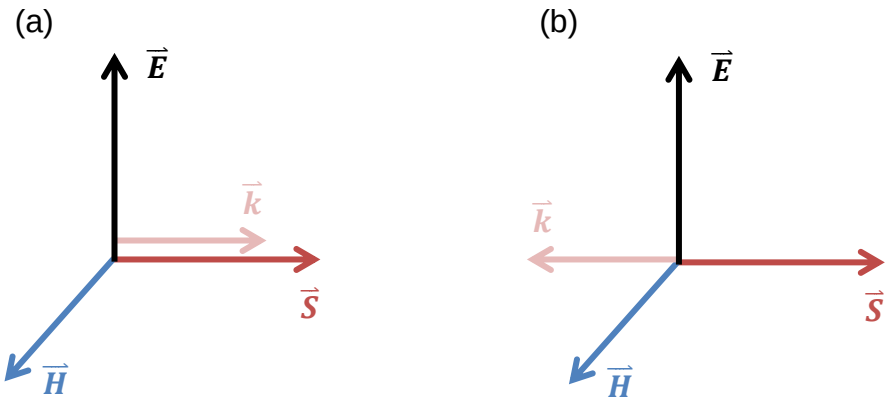

Figure 3.1.1. (a) Positive index media (ε and $\mu > 0$) exhibit a right-handed relationship between the vector set $\{\vec{k}, \vec{E}, \vec{H}\}$ and wavevector $\vec{k}$ is parallel to the Poynting vector $\vec{S}$. (b) For negative index media (ε and $\mu < 0$), $\{\vec{k}, \vec{E}, \vec{H}\}$ forms a left-handed set and $\vec{k}$ is perpendicular to the direction of energy flux $\vec{S}$.

The effect of negative index on other material parameters can be determined through similar means. Consider, for example, Snell’s Law [62]:

$$\frac{\sin\theta_1}{\sin\theta_2} = \frac{n_1}{n_2}, \qquad 3.1.4$$

which describes the angle at which light is bent (θ_2) as it travels from medium 1 (with angle of incidence θ_1) into medium 2. When one of the two media is replaced with a NIM, Eqn. 3.1.4 is still satisfied, but under strange conditions: Snell's law for light traveling from a positive index medium (n_+ with angle θ_+) into a negative index medium (n_-) bends at the following angle

$$\theta_- = \sin^{-1}\left(\frac{\sin\theta_+ n_-}{n_+}\right). \qquad 3.1.5$$

Here, the direction of the light ray in the NIM is mirrored about the surface normal compared to the positive index case, as depicted in Fig. 3.1.2.

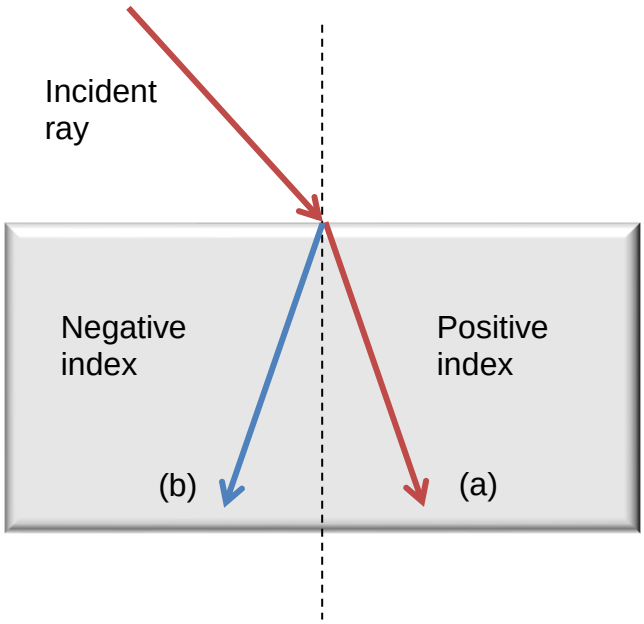

Figure 3.1.2. Snell's Law, illustrated for an incident ray (red) traveling from one positive medium into (a) another positive medium and (b) a negative medium. Apparently, the direction the ray is bent is directly inverted in a negative index material.

As a consequence of their potential for bending light in non-standard ways, Veselago's suggested in his original paper that NIM could be used as a so-called "superlens". The principle is illustrated in Fig. 3.1.3. Little else was said regarding the use of NIM as lenses until 2000, when J. B. Pendry posited that a negative index material slab could be used as a perfect lens – that is, a lens capable of overcoming the diffraction limit, allowing for the resolution of sub-wavelength features [63]. Briefly, to understand how planar NIM are able to focus light, consider a source some distance d from a negative-positive index interface. As dictated by Snell's Law, light impinging on the interface and entering the negative material will be refracted at an angle of $-\theta_{-}$ with respect to the surface normal. If the width of the NIM w is such that $w > d$, the light focuses within the medium and subsequently diverges until it reaches the second interface. Here, the light is refracted back at an angle of $+\theta_{+}$ in the positive medium, where it reaches a second focus at distance that $w - d$ from the interface. This refocusing effect is made possible by a phase reversal that occurs within the medium, as demonstrated by the transmission coefficient T. Taking propagation along $\hat{z}$, the transmission coefficient through the medium is given by

$$T = e^{ik_z' d} = e^{-i\sqrt{\omega^2 c^2 - k_x^2 - k_y^2}\, d} \qquad 3.1.6$$

where the sign reversal $(k_z \rightarrow -k_{x,y})$ is a natural consequence of the propagation direction opposing the direction of energy flow $(+k)$ [60].

To demonstrate sub-wavelength imaging capabilities of such a NIM slab, Pendry calculated the transmission coefficients for the cases of both *S*- and *P*-polarized waves traveling through the slab. In vacuum, the evanescent components of the waves have imaginary wavevectors ik_z such that the waves are defined by $\exp(i(ik_z)z) = \exp(-kz)$.

For the case of negative index, Pendry showed that, in theory, the transmission coefficient for either *S*- or *P*-polarized waves through the slab scale as $\exp(-ik_z d)$ and so are amplified within the medium. Now, both propagating and evanescent waves factor into the image resolution, and, as sub-wavelength information is carried within the evanescent component, the diffraction limit is effectively circumvented.

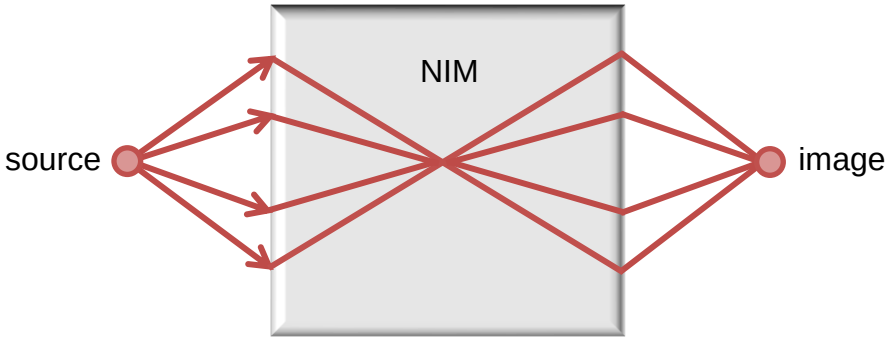

Figure 3.1.3. Refraction of light at a positive-negative index interface causes the ray to bend at a negative angle with respect to the surface normal. If the thickness of the material is chosen such that it is larger than the distance between the source and interface, the light will converge within the medium, diverge until it reaches the second interface, and subsequently re-focus at a second point. Adapted from [64].

Materials demonstrating simultaneously negative ε and μ have yet to be found in nature. Instead, these parameters are achieved by highly structured meta-materials. Metamaterials are manmade structures consisting of repeating subunits whose construction based on the application at hand – for example, small metal spheres are used to increase the dielectric response beyond natural materials, while split-ring resonators are used to achieve artificial magnetism [65]. Typically, a large number of

subunits are stacked together along the wave propagation directions, in approximation of a homogenous medium, to generate appreciable material response.

Even in artificially engineered metamaterials, the condition for negative index, that both ε and μ be simultaneously negative, has proven difficult to achieve experimentally. Though there are several ways to obtain negative ε [66] and μ [67, 68] independently, obtaining both for the same frequency range (particularly in the visible regime) has proven challenging. Many of these approaches attempt merely to hybridize standard negative ε materials (such as thin wire media) with negative ε materials (like the split-ring resonators). In each case, the media are highly lossy and have only a narrow range of frequencies for which both ε and μ are negative, limiting their applications to rather specific instances [69, 70, 71].

In the rest of this chapter, a method for generating NIM through use of a bi-isotropic (BI) medium is explored. Though BIM have been vaguely identified as a possible candidate for generating NIM, no suitable materials have yet been identified. By making connections between the multipolar terms derived in Chapter 2 and the well-known material parameters of electromagnetism, it becomes clear that uniaxial scatterers such as the dimer nantenna present an attractive and readily realizable alternative to the previous NI methods.

3.2: Generalization Using Constitutive Equations

From inspection of the effective sample scattering matrix given in Eqn. 2.7.3b, it is evident that two terms generate electromagnetic cross coupling: the linear (mq) and circular (md) dichroism. A material comprised of such uniaxial scatters will then be, in

the most general case, *bi-isotropic* (BI). For a general BI medium, this cross coupling between the electric and magnetic field components in the medium is described by the well-known constitutive equations [60]

$$\vec{B} = \mu\vec{H} + (\chi + i\kappa)\vec{E} \qquad 3.2.1a$$

$$\vec{D} = \varepsilon\vec{E} + (\chi - i\kappa)\vec{H} \qquad 3.2.1b$$

where χ and κ are the dimensionless non-reciprocal and chiral terms, respectively, and ε and μ are the standard electric permittivity and magnetic permeability, respectively. Essentially, Eqns. 3.2.1a-b indicate that the electric field induces magnetic polarization in the medium, and the magnetic field induces electric polarization. Indeed, if χ and κ are set to zero in the above equations, they return to the standard constitutive equations for linear media. While a general BI material has both χ and κ, two important subclasses emerge based on their values. These are described in detail in the proceeding sections.

1. Materials with $\chi \neq 0$ and $\kappa = 0$ are called Tellegen media and are characterized by their non-reciprocal, achiral response. Here, the electric response in the medium induces a change in the magnetic component (and so is called an electromagnetic effect). One of the most striking effects of such a coupling is the backward propagation of waves within the medium. The existence of pure Tellegen media has been heavily debated int eh past 20 years (in fact, one of the first links on a Google search of “Tellegen Media” is called *Do Tellegen particles really exist?* [72]).
2. Materials with $\kappa \neq 0$ and $\chi = 0$ are called Pasteur media and are characterized by their chiral, reciprocal response. In chiral media, the magnetic component of the field induces a magnetic current, which in turn affects the electric component of the field

(magnetoelectric effect). Chiral object, from molecules to metamaterials, have been an area of active research since their first description by Lord Kelvin over 100 years ago.

3.3: Wave Propagation and Negative Index in Bi-Isotropic Media

One of the most immediate features of BI media is their birefringence – *e.g.*, polarization-dependent refractive index. To see this clearly, a simple derivation of the wave propagation in BI media, leading to split index of refraction, is presented here. Starting with the source-free Faraday and modified Ampere's laws from the Maxwell Equations [73]:

$$\vec{\nabla} \times \vec{E} = -\frac{\partial}{\partial t}\vec{B} \qquad 3.3.1a$$

$$\vec{\nabla} \times \vec{H} = \frac{\partial}{\partial t}\vec{D}. \qquad 3.3.1b$$

Inserting the BI constitutive equations (Eqn. 3.2.1a into Eqn. 3.3.1a and Eqn. 3.2.1b into Eqn. 3.3.1b) gives, respectively,

$$\vec{\nabla} \times \vec{E} = -(\chi + i\kappa)\frac{\partial}{\partial t}\vec{E} - \mu\frac{\partial}{\partial t}\vec{H} \qquad 3.3.2a$$

$$\vec{\nabla} \times \vec{H} = (\chi - i\kappa)\frac{\partial}{\partial t}\vec{H} + \varepsilon\frac{\partial}{\partial t}\vec{E}. \qquad 3.3.2b$$

Now, taking the curl of Eqn. 3.3.2a, and noting that the curl commutes with the time derivative $\left(\left[\frac{\partial}{\partial t}, \vec{\nabla}\times\right] = 0\right)$,

$$\vec{\nabla} \times \vec{\nabla} \times \vec{E} = -(\chi + i\kappa)\frac{\partial}{\partial t}\vec{\nabla} \times \vec{E} - \mu\frac{\partial}{\partial t}\vec{\nabla} \times \vec{H} \qquad 3.3.3$$

and substituting Eqn. 3.3.2b gives

$$\vec{\nabla} \times \vec{\nabla} \times \vec{E} = -(\chi + i\kappa)\frac{\partial}{\partial t}\vec{\nabla} \times -\mu\varepsilon\frac{\partial^2}{\partial t^2}\vec{E} - (\chi - i\kappa)\frac{\partial}{\partial t}\left(\frac{\partial}{\partial t}\mu\vec{H}\right). \qquad 3.3.4$$

Rearranging Eqn. 3.3.2a in terms of $\mu\vec{H}$ and inserting into Eqn. 3.3.4 above yields, finally,

$$\vec{\nabla}\times\vec{\nabla}\times\vec{E} = -(\chi+i\kappa)\frac{\partial}{\partial t}\vec{\nabla}\times\vec{E} - \mu\varepsilon\frac{\partial^2}{\partial t^2}\vec{E} - (\chi-i\kappa)\frac{\partial}{\partial t}\left[-\vec{\nabla}\times\vec{E} - (\chi+i\kappa)\frac{\partial}{\partial t}\vec{E}\right]$$

$$= -2i\kappa\frac{\partial}{\partial t}\vec{\nabla}\times\vec{E} + (\chi^2+\kappa^2-\mu\varepsilon)\frac{\partial^2}{\partial t^2}\vec{E}. \quad 3.3.5$$

Based on the definition of the Fourier Transform, $\frac{\partial}{\partial t} = \omega$, Eqn. 3.3.5 can be written

$$0 = \vec{\nabla}\times\vec{\nabla}\times\vec{E} + 2i\kappa\omega\vec{\nabla}\times\vec{E} - \omega^2(\chi^2+\kappa^2-\mu\varepsilon)\vec{E}. \quad 3.3.6$$

Eqn. 3.3.6 describes the propagation of electromagnetic waves in the BI medium, which is governed by the solutions

$$k_\pm = \omega\left(\sqrt{\mu\varepsilon-\chi^2}\pm\kappa\right) \quad 3.3.7$$

with corresponding refractive indices $n = k/\omega$ of

$$n_\pm = \sqrt{\mu\varepsilon-\chi^2}\pm\kappa. \quad 3.3.8$$

Inspection of Eqn. 3.3.8 reveals immediately the advantage of BI media: namely, that the conditions necessary for generating negative refractive index are significantly relaxed compared to the standard double-negative material ($\varepsilon=\mu=0$). If $|\kappa| > \sqrt{\varepsilon\mu-\chi^2}$, the index is inherently negative for k_-. Though not necessary, the inclusion of non-zero χ further relaxes the conditions as smaller values of κ now lead to $-n$, as compared to those required for Pasteur media.

To case these results in terms of the excitable plasmonic modes $\{d,q,m\}$ of the dimer nantenna, we return to the effective interaction matrix of Eqn. 2.7.3b:

$$\Sigma_x = \begin{pmatrix} d^2+q^2 & mq-imd \\ mq+imd & m^2 \end{pmatrix}. \quad 3.3.9$$

Based on the bi-isotropic nature of the interaction, the output polarization goes succinctly as

$$\begin{pmatrix} D \\ B \end{pmatrix} = \begin{pmatrix} d^2 + q^2 & mq - imd \\ mq + imd & m^2 \end{pmatrix} \begin{pmatrix} E \\ H \end{pmatrix} \tag{3.3.10}$$

which is analogous to the constitutive equations, cast into matrix representation as

$$\begin{pmatrix} D \\ B \end{pmatrix} = \begin{pmatrix} \varepsilon & \chi - i\kappa \\ \chi + i\kappa & \mu \end{pmatrix} \begin{pmatrix} E \\ H \end{pmatrix}. \tag{3.3.11}$$

By comparison of the constitutive relations with the sample scattering matrix above, the material parameters $\{\varepsilon, \mu, \chi, \kappa\}$ are equated with the multipolar resonances $\{d, q, m\}$ as

$$\varepsilon = d^2 + q^2 \tag{3.3.12a}$$

$$\mu = m^2 \tag{3.3.12b}$$

$$\chi = mq \tag{3.3.12c}$$

$$\kappa = md \tag{3.3.12d}$$

with split refractive index (from Eqn. 3.3.8)

$$n_{\pm} = \sqrt{(d^2 + q^2)m^2 - (mq)^2} \pm md = md \pm md. \tag{3.3.13}$$

The final indices, n_+ and n_-, are then given by

$$n_+ = 2md = 2\kappa \tag{3.3.14a}$$

$$n_- = 0 \tag{3.3.14b}$$

with corresponding propagation factors $k_+ = 2\omega md$ and $k_- = 0$. Evidently only one Eigenmode (here, k_+, typically distinguished as right-handed circularly polarized light) propagates within the medium, with the sign of the index defined solely by that of m relative to d. The effect of non-reciprocity, while interesting in its own right, does not explicitly factor into the final index.

This is a particularly interesting case of chirality *only* defining the index of refraction, one that is distinct from chiral nihility where $\varepsilon = \mu = 0$ but $\kappa \neq 0$ – both ε and μ still exist, they have just canceled out. In the case of formal chiral nihility, negative index is indeed achievable but there are still two Eigenmodes that persist in the material with equal but opposite propagation constants. Here, only one mode persists while the other is entirely attenuated.

3.4: Applications

The most immediate application of such a material is in the generation of orientation-dependent negative index films. Given that the sign of md and thus, handedness, of the dimers is defined by their orientation, a simple in-plane rotation will take the film from positive to negative index continuously. In this case, the material would consist of stacked films, with each film containing an array of nanodimers embedded in a non-interfering matrix (such as silicon nitride or sol-gel). As the junction asymmetry is what dictates the handedness at a given orientation, dimers can be batch fabricated to have identical structural features. One method of doing this is through photolithography, which has been extensively used to generate asymmetric structures of various shapes and sizes.

Though such a film would only display variable index under CPL, it shows a much broader active spectral range than previously reported materials. As shown in Fig. 3.4.1, gold nanodimers have a large scattering cross section (which is necessary to generate the large SERS-based chirality) that extends throughout the near-UV and into the visible and near-IR range [58].

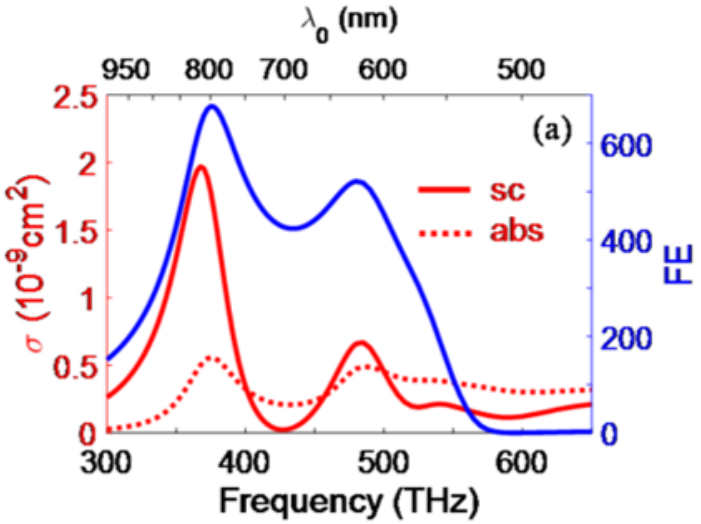

Figure 3.4.1. Scattering and absorption cross-section (red) and field enhancement (blue) spectrum of a symmetric nanodimer excited with light polarized along its long (inter-particle) axis. Reprinted with permission from [58].

In addition to the negative index that can be sustained in such media, the zero-index mode is of equal interest as it has applications in optical circuits and quantum computing. Further studies will have to be done to verify the validity of these indices, but the treatment here has provided a general proof-of-concept that illustrates the utility plasmonic nantenna have in the world of metamaterials and applied optoelectronics.

CHAPTER 4: Summary and Conclusions

The confusion regarding the appearance of backgrounds in SERS spectra has been resolved here through careful disentanglement of the metallic and molecular response of the decorated nantenna. This work has shown that the background can be assigned to inelastic light scattering on the gold nantenna itself, which has been termed electronic Raman scattering (ERS). Upon this realization, information such as metallic and molecular temperature can be cleanly extracted directly from the SERS spectra. Additionally, experiments into the power dependence of SERS spectra reveal that while the metal response increases linearly with excitation intensity, the non-linear response in the molecular lines can be treated by consideration of the molecular partition function. Finally, while ERS can be described straightforwardly by consideration of the population of thermal hole states (which serve as the terminal state in the ERS process), a richer wealth of information is provided through the full quantum mechanical treatment that was presented here.

Furthermore, the phenomena of ODH and chiral connectedness and the distinction between chirality and handedness find satisfactory resolution in the presented CD and LD measurements on individual nantenna. The contradiction of a nominally achiral structure showing giant optical activity does not have a formal resolution, due to the lack of a quantitative continuous measure of chirality. The challenge may be reduced to the more mundane question of how spherical (achiral) is a nanosphere? The typical gold nanosphere of ~50 nm radius fails to qualify, as evidenced by the giant chiroptical response of its dimer. Besides the gross size scale $\zeta \approx 1$ essential for retardation to play a role, nanostructuring on much finer scale controls

the definite handedness of their interaction with light. This is ultimately traced to the broken degeneracy of $\Lambda \neq 0$ plasmons, which emerges from the treatment of dichroism as the quantum interference between resonantly prepared electric and magnetic plasmons. although the treatment is formally first order in the spatial dispersion [74], terms up to ζ^4 contribute to the dichroism in the limit $\zeta \approx 1$. This generates previously unexplored rich physics and suggests the manipulation of quantum superpositions of plasmons as a powerful paradigm for novel materials applications. A more specific application of chiral plasmons is to amplify the CD of molecules, which otherwise is a feeble effect in the $\zeta \ll 1$ limit [75-78]. Rather than molecular activity, polarization-based methods are likely to probe the nantenna. Chiral induction should be possible to transfer from the vortex core of plasmons to molecules located at the nanojunction, where a second scaling factor applies: $\zeta_g = 2\pi r/g$, given by molecular dimensions, r, and gap length, g. This information is encoded in the spectra, as already realized by the observation of magnetic and quadrupolar vibrational Raman spectra at the hot spot of nanojunctions [23]. There will be a significant concentration of chiral current and vorticity at the junction, with associated large optomagnetic dipoles and monopoles that should be possible to harness. A fully quantum treatment of plasmonics on irregular structures would be invaluable for a rigorous understanding of their dynamics and control over their active optical response.

APPENDIX

A1. Light-Matter Interaction Derivation

The goal here is to determine the nature of the quantum mechanical modes of the scatterer that couple to the exciting field. The general form of the light-matter interaction potential, which mediates the material response, is given by [9]:

$$\hat{V} = \frac{i\hbar e}{2m}\left(\vec{\nabla}\cdot\vec{A} + \vec{A}\cdot\vec{\nabla}\right) + \frac{e^2}{2mc^2}\vec{A}\cdot\vec{A}. \quad \text{A1.1}$$

The second term arises from an interaction that does not induce any change in energy – it is an elastic process and therefore attributable to Rayleigh scattering. As the primary interest of this treatment is in the inelastic Raman process, the second term is ignored and the derivation will proceed with the first term only. In the Coulomb gauge, $\vec{\nabla}\cdot\vec{A} + \vec{A}\cdot\vec{\nabla} = 2\vec{A}\cdot\vec{\nabla}$, and so Eqn. A1.1 becomes

$$\hat{V} = \frac{i\hbar e}{m}\vec{A}\cdot\vec{\nabla}. \quad \text{A1.2}$$

The vector potential $\vec{A}$ is in the form of a plane wave and therefore given straightforwardly by $\vec{A} = A_0 e^{i(k\cdot r - \omega t)}$. With this in hand, the now-oscillatory Eqn. A1.2 can be input into to Fermi's Golden Rule which allows for identification of the allowable transitions (from $b \to a$).

$$\langle b|V(t)|a\rangle = \frac{i\hbar e}{m}A_0 e^{-i\omega t}\left\langle b\middle|e^{ik\cdot r}\cdot\vec{\nabla}\middle|a\right\rangle \quad \text{A1.3}$$

For simplicity, the problem will be reduced to two dimensions with propagation along $\hat{z}$ ($\vec{k} = k_z\hat{z}$) and polarization along $\hat{x}$ $\left(\vec{\nabla} = \frac{\partial}{\partial x}\right)$:

$$\langle b|V(t)|a\rangle = \frac{i\hbar e}{m}A_0 e^{-i\omega t}\left\langle b\middle|e^{ikz}\cdot\frac{\partial}{\partial x}\middle|a\right\rangle \quad \text{A1.4}$$

Typically, the spatial portion of the vector potential $e^{ik\cdot r}$ is taken only to zeroth order, $e^{ik\cdot r} \approx 1$, due to size considerations. This holds true for the case of molecular scattering, where the size of the object (~1 nm) is much smaller than the k-vector of the field and $k \cdot r = \frac{2\pi r}{\lambda} \sim 0$. This is the basis for the dipolar approximation that predicates much of molecular Raman theory. For the case of the 100 nm dimers, however, this assumption is no longer valid as $\frac{2\pi r}{\lambda} \sim 1$ – spatial dispersion cannot be ignored here, and to that end the vector potential is expanded to first order in spatial dispersion: $e^{ik\cdot r} \approx 1 + ik \cdot r = 1 + ikz$. This expansion serves as the basis for multipolar Raman scattering, and is necessary to justify the observed dichroism. Using this, A1.3 becomes

$$\langle b|V(t)|a\rangle = \frac{i\hbar e}{m} A_0 e^{-i\omega t} \left\langle b\middle|(1 + ikz) \cdot \frac{\partial}{\partial x}\middle|a\right\rangle \quad \text{A1.5a}$$

$$= \frac{i\hbar e}{m} A_0 e^{-i\omega t} \left[\left\langle b\middle|\frac{\partial}{\partial x}\middle|a\right\rangle + ik \left\langle b\middle|z \cdot \frac{\partial}{\partial x}\middle|a\right\rangle\right]. \quad \text{A1.5b}$$

Working first with the zeroth-order electric dipole term, the first term in the brackets of Eqn. A1.5b. The spatial derivative is transformed by the commutator of the Hamiltonian and position operator, by recognizing that $\left[\hat{H}, \hat{x}\right] = -\frac{i\hbar}{m}\hat{p}_x = -\frac{\hbar^2}{m}\frac{\partial}{\partial x}$ so that

$$\left\langle b\middle|\frac{\partial}{\partial x}\middle|a\right\rangle = -\frac{m}{\hbar^2}\langle b|Hx - xH|a\rangle. \quad \text{A1.6}$$

The Hamiltonian effectively picks the energy of states a, b so that Eqn. A1.6 becomes

$$\left\langle b\middle|\frac{\partial}{\partial x}\middle|a\right\rangle = -\frac{m}{\hbar^2}\langle b|E_b x - xE_a|a\rangle. \quad \text{A1.7}$$

Now, defining the energy difference in terms of frequency $E_b - E_a = \hbar\omega_{ba}$ allows Eqn. A1.7 to simplify to

$$\left\langle b\left|\frac{\partial}{\partial x}\right|a\right\rangle = -\frac{m\omega_{ba}}{\hbar}\langle b|x|a\rangle \qquad \text{A1.8}$$

For the second term in A1.5b, start by adding zero in the form of $x\frac{\partial}{\partial x}$:

$$\left\langle b\left|z\cdot\frac{\partial}{\partial x}\right|a\right\rangle = \frac{1}{2}\left\langle b\left|z\cdot\frac{\partial}{\partial x} - x\cdot\frac{\partial}{\partial z}\right|a\right\rangle + \frac{1}{2}\left\langle b\left|z\cdot\frac{\partial}{\partial x} + x\cdot\frac{\partial}{\partial z}\right|a\right\rangle. \qquad \text{A1.9}$$

These terms correspond, respectively, to the magnetic dipole and electric quadrupole excitations. To see this more clearly, working first with the magnetic dipole term and using $p_j = -i\hbar\frac{\partial}{\partial j}$:

$$\begin{aligned}\frac{1}{2}\left\langle b\left|z\cdot\frac{\partial}{\partial x} - x\cdot\frac{\partial}{\partial z}\right|a\right\rangle &= -\frac{1}{2i\hbar}\left\langle b\left|z\left(-i\hbar\frac{\partial}{\partial x}\right) - x\left(-i\hbar\frac{\partial}{\partial z}\right)\right|a\right\rangle \\ &= \frac{i}{2\hbar}\langle b|zp_x - xp_z|a\rangle = \frac{i}{2\hbar}\left\langle b\left|\hat{L}_y\right|a\right\rangle \qquad \text{A1.10}\end{aligned}$$

Where $zp_x - xp_z$ has been identified as the angular momentum operator, $\hat{L}_y$. For the quadrupolar term, the commutator $\left[\hat{H},\hat{j}\right]$ is once again called upon:

$$\begin{aligned}\frac{1}{2}\left\langle b\left|z\cdot\frac{\partial}{\partial x} + x\cdot\frac{\partial}{\partial z}\right|a\right\rangle &= -\frac{m}{2\hbar^2}\langle b|Hxz - zxH|a\rangle \\ &= -\frac{m\omega_{ba}}{2\hbar}\langle b|xz|a\rangle \qquad \text{A1.11}\end{aligned}$$

Taking all three terms together, from Eqns. A1.8, A1.10, and A1.11, and substituting back into Eqn. A1.5b gives

$$\langle V\rangle = \frac{i\hbar e}{m}A_0 e^{-i\omega t}\left[-ie\omega_{ba}\langle b|x|a\rangle - \frac{ike}{2m}\left\langle b\left|\hat{L}_y\right|a\right\rangle + \frac{ek\omega_{ba}}{2}\langle b|xz|a\rangle\right]. \qquad \text{A1.12}$$

From this, the three terms are readily recast using the standard definitions for the electric dipole, magnetic dipole, and electric quadrupole: $ex = \mu_e, \frac{eL}{2} = \mu_m, exz = q_{xz}$.

The symmetric nature of the transitions is also invoked here to transform $\omega_{ba} = -\omega_{ab}$.

In total, Eqn. A1.12 (with a little regrouping) now becomes

$$\langle V\rangle = i\omega_{ab}A_0 e^{-i\omega t}\left(\langle b|\mu_e|a\rangle - \frac{k}{\omega_{ab}}\langle b|\mu_m|a\rangle + \frac{ik}{2}\langle b|q_{xz}|a\rangle\right). \qquad \text{A1.13}$$

Recall that the quantum mechanical definition for the orbital angular momentum operator is inherently complex as it contains a linear momentum term ($\hat{L} = \vec{r} \times \vec{p}$). Forcing this term to be real by extracting the $-i$ yields finally

$$\langle V \rangle = i\omega_{ab} A_0 e^{-i\omega t} \left(\langle b|\mu_e|a\rangle + \frac{ik}{\omega_{ab}} \langle b|\mu_m|a\rangle + \frac{ik}{2} \langle b|q_{xz}|a\rangle \right). \quad \text{A1.14}$$

The derivation of Eqn. A1.14 in three dimensions is show explicitly in [Schatz & Ratner]. Here, the polarization is generalized into the vector $\hat{\epsilon}$, and the transition elements into corresponding vectors $\left(\vec{d}, \vec{m}\right)$ and dyadic (q_{ba}); all prefactors remains the same. Using this, Eqn. A1.13 is transformed into three dimensions as

$$\langle V \rangle = i\omega_{ab} A_0 e^{-i\omega t} \left(\hat{\epsilon} \cdot \vec{d} + \frac{i}{\omega_{ab}} \vec{k} \times \hat{\epsilon} \cdot \vec{m} + \frac{i}{2} \hat{\epsilon} \cdot \vec{q} \cdot \vec{k} \right) \quad \text{A1.15}$$

As $\omega = \omega_{ab}$ on resonance and $\vec{E} = -\frac{\partial}{\partial t}\vec{A}$, the quantity to the left of the parenthesis becomes $\vec{E}(t)$. Scaling all terms left inside the parenthesis by the electric dipole leads to the unitless interaction potential:

$$\langle V \rangle \sim \hat{\epsilon} \cdot \hat{d} + \frac{i}{2} \left(\zeta_m \hat{k} \times \hat{\epsilon} \cdot \hat{m} + \zeta_q \hat{\epsilon} \cdot \hat{q} \cdot \hat{k} \right)$$

A2. Jones Matrices and Optical Trains

A2.1 HWP (LD) experiment

The HWP experiment consists of sending linearly polarized light through a rotating HWP, interacting with the sample, and decomposing the scattered signal onto a pair of orthogonal channels: one parallel to the incident polarization, and one perpendicular to it. This can be represented concisely by a rotating polarization state of incident light (starting horizontally polarized at $\varphi = 0°$):

$$\epsilon_{in}(\varphi) = \begin{pmatrix} \epsilon_x(\varphi) \\ \epsilon_y(\varphi) \end{pmatrix} = \begin{pmatrix} \cos\varphi \\ \sin\varphi \end{pmatrix}$$

The parallel and perpendicular channels are then defined as beig aligned and orthogonal to $\epsilon_{in}(\varphi)$, respectively:

$$\epsilon_{para}(\varphi) = \begin{pmatrix} \cos\varphi \\ \sin\varphi \end{pmatrix}$$

$$\epsilon_{perp}(\varphi) = \begin{pmatrix} -\sin\varphi \\ \cos\varphi \end{pmatrix}$$

where the negative sign in ϵ_{perp} is required to ensure orthogonality of the channels, $\epsilon_{para} \cdot \epsilon_{perp} = 0$. Recall that measurements are made on the total intensity of the interaction, which is the square modulus of the field. Using the sample matrix α (Eqn. 2.2.9), the measurement in the two channels can be constructed as

$$I_{para}(\varphi) = \left|\epsilon_{para}(\varphi) \cdot \alpha \cdot \epsilon_{in}(\varphi)\right|^2$$

$$= d^2 \cos\varphi^2 \left((d^2 + q^2)\cos\varphi^2 - 2mq\cos\varphi\sin\varphi + m^2\sin\varphi^2\right)$$

$$I_{perp}(\varphi) = \left|\epsilon_{perp}(\varphi) \cdot \alpha \cdot \epsilon_{in}(\varphi)\right|^2$$

$$= d^2\left((d^2 + q^2)\cos\varphi^2\sin\varphi^2 - 2mq\cos\varphi\sin\varphi^3 + m^2\sin\varphi^4\right)$$

A2.2 QWP (CD) experiment

The QWP experiment consists of sending linearly polarized light through a rotating QWP, interacting with the sample, and measuring the total scattered signal (no channel decomposition here). The input field ϵ_{in} is succinctly represented by sending horizontally polarized light ϵ_h through an initially horizontal QWP, which is then rotated in angle φ, $Q_h(\varphi)$:

$$\epsilon_{in}(\varphi) = Q_h(\varphi)\cdot\epsilon_h = \left(R_\varphi^T\cdot Q_h\cdot R_\varphi\right)\cdot\epsilon_h$$

$$= \left(\begin{pmatrix}\cos\varphi & \sin\varphi\\ -\sin\varphi & \cos\varphi\end{pmatrix}\cdot e^{\frac{i\pi}{4}}\begin{pmatrix}1 & 0\\ 0 & i\end{pmatrix}\cdot\begin{pmatrix}\cos\varphi & \sin\varphi\\ \sin\varphi & \cos\varphi\end{pmatrix}\right)\cdot\begin{pmatrix}1\\0\end{pmatrix}$$

$$= \begin{pmatrix}\left(1/\sqrt{2}\right)(1+\cos(2\varphi))\\ -\sqrt{2}\cos\varphi\sin\varphi\end{pmatrix}$$

This input field is then incident on the sample, described by matrix α, given a total intensity that is described as follows.

$$I_{QWP}(\varphi) = |\alpha\cdot\epsilon_{in}(\varphi)|^2$$

$$= \frac{d^2}{2}\left((d^2+q^2)(1+\cos(2\varphi)^2)\right.$$

$$\left.+\,2m(d+q\cos(2\varphi))\sin(2\varphi)+m^2\sin(2\varphi)^2\right)$$

A3. List of Abbreviations Used Throughout

Greek and Roman Characters

χ……..... non-reciprocal (Tellegen) parameter
c……. speed of light
d……..... electric dipole
E, ϵ…….……electric field
ε……..……electric permittivity
H, h…….magnetic field
i…….…….. imaginary number
k……..……wavevector
κ……. chiral (Pasteur) parameter
m…….…….. magnetic dipole
n……index of refraction
$\bar{\nu}$……. wavenumber (cm^{-1})
ω…… frequency (s^{-1})
μ……. magnetic permeability
q……. electric quadrupole

Mathematical Operations

$\vec{\nabla}\times$……. curl
$\frac{\partial}{\partial t}$…… time derivative
$[a, b]$……..... commutator of a and b
$\hat{P}$…….....parity operator, which inverts spatial coordinates
$\hat{T}$…….....timer reversal operator, which imparts a complex conjugation

Abbreviations and Acronyms

AS……..anti-Stokes
BI……bi-isotropic
BPE……..... bipyridyl ethylene
CD……..... circular dichroism
CP……..... circularly polarized
CW……..... continuous wave
ERS……..... electronic Raman scattering
fs……..... femtosecond
HWP…….....halfwave plate
LCP……..... left circularly polarized light
LD…….....linear dichroism
LH…….....left handed
LP…….....linear polarizer

NDF……neutral density filter
NF……..... notch filter
NIM…… negative index media/material
nm……..... nanometer
μm……..... micron
μW…….....micro-Watt
PBS……..... polarized beam splitter
QWP…….....quarterwave plate
RCP…….....right circularly polarized light
RH……..... right handed
SERS…….....surface enhanced Raman scattering
SP…… surface plasmon

REFERENCES

[1] Fleischmann, M.; Hendra, P. J.; McQuillan, A. J. Raman Spectra of Pyridine Adsorbed at a Silver Electrode. *Chem. Phys. Lett.* **1974**, *26*, 163-166.

[2] De Silva, I. A. S.; Fabris, L. SERS-Based Approaches Toward Genetic Profiling. *Bioanalysis* **2015**, *7*, 263-278.

[3] Granger, J. H.; Granger, M. C.; Firpo, M. A.; Mulvihill, S. J.; Porter, M. D. Toward Development of a Surface-Enhanced Raman Scattering (SERS)-Based Cancer Diagnostic Immunoassay Panel. *Analyst* **2013**, *2*, 410-416.

[4] Sharma, B.; Frontiera, R. R.; Henry, A.-I.; Ringe, E.; Van Duyne, R. P. SERS: Materials, Applications, and the Future. *Materials Today* **2012**, *15*, 16-25.

[5] Alu, A.; Egheta, N. Hertzian Plasmonic Nanodimer as an Efficient Optical Nanoantenna. *Phys. Rev. B* **2008**, *78*, 1-6.

[6] Zhang, T.; Lu, G.; Shen, H.; Shi, K.; Jiang, Y.; Xu, D.; Gong, Q. Photoluminescence of a Single Complex Plasmonic Nanoparticle. *Sci. Rep.* **2014**, *4*, 3867

[7] Mahajan, S.; Cole, R. M.; Speed, J. D.; Pelfrey, S. H.; Russell, A. E.; Bartlett, P. N.; Barnett, S. M.; Baumberg, J. J. Understanding the Surface-Enhanced Raman Spectroscopy “Background”. *J. Phys. Chem. C* **2010**, *114*, 7242– 7250.

[8] Laurent, G.; Félidj, N.; Aubard, J.; Lévi, G.; Krenn, J. R.; Hohenau, A.; Schider, G.; Leitner, A.; Aussenegg, F. R. Evidence of Multipolar Excitations in Surface Enhanced Raman Scattering. *Phys. Rev. B*. **2005**, *71*.

[9] Schatz, G. C; Ratner, M. A. *Quantum Mechanics in Chemistry*, 1st ed.; Dover: New York, 2002.

[10] Barron, L. D.; Hecht, L.; Blanch, E. E.; Bell, A. F. Solution Structure and Dynamics of Biomolecules from Raman Optical Activity. *Prog. Biophys. Mol. Biol.* **2000**, *73*, 1-49.

[11] Novotny, L.; van Hulst, N. F. Antennas for Light. *Nat. Photonics* **2011**, *5*, 83–90.

[12] Jeanmaire, D. L.; Duyne, R. P. Van. Surface Enhanced Raman Spectroelectrochemistry. *J. Electroanal. Chem.* **1977**, *84*, 1–20.

[13] Kneipp, K., Moskovits, M., Kneipp, H. *Surface-Enhanced Raman Scattering: Physics and Applications*, 1st ed.; Springer: Heidelberg, 2010.

[14] Nie, S.; Emory, S. R. Probing Single Molecules and Single Nanoparticles by Surface-Enhanced Raman Scattering. *Science* **1997**, *275*, 1102–1106.

[15] Kneipp, K.; Wang, Y.; Kneipp, H.; Perelman, L.; Itzkan, I.; Dasari, R.; Feld, M. Single Molecule Detection Using Surface-Enhanced Raman Scattering (SERS). *Phys. Rev. Lett.* **1997**, *78*, 1667–1670.

[16] Blackie, E. J.; Le Ru, E.; Etchegoin, P. G. Single-Molecule Surface-Enhanced Raman Spectroscopy of Nonresonant Molecules. *J. Am. Chem. Soc.* **2009**, *131*, 14466–14472.

[17] Haran, G. Single-Molecule Raman Spectroscopy: A Probe of Surface Dynamics and Plasmonic Fields. *Acc. Chem. Res.* **2010**, *43*, 1135–1143.

[18] Le Ru, E.; Etchegoin, P. G. Single-Molecule Surface-Enhanced Raman Spectroscopy. *Annu. Rev. Phys. Chem* **2012**, No. December 2011, 1–23.

[19] Yampolsky, S.; Fishman, D. A.; Dey, S.; Hulkko, E.; Banik, M.; Potma, E. O.; Apkarian, V. A. Seeing a Single Molecule Vibrate through Time-Resolved Coherent Anti-Stokes Raman Scattering. *Nat. Photonics* **2014**, *8*, 650–656.

[20] Camden, J. P.; Dieringer, J. a; Wang, Y.; Masiello, D. J.; Marks, L. D.; Schatz, G. C.; Van Duyne, R. P. Probing the Structure of Single-Molecule Surface-Enhanced Raman Scattering Hot Spots. *J. Am. Chem. Soc.* **2008**, *130*, 12616–12617.

[21] Dadosh, T.; Sperling, J.; Bryant, G. W.; Breslow, R.; Shegai, T.; Dyshel, M.; Haran, G.; Bar-Joseph, I. Plasmonic Control of the Shape of the Raman Spectrum of a Single Molecule in a Silver Nanoparticle Dimer. *ACS Nano* **2009**, *3*, 1988–1994.

[22] Camargo, P. H. C.; Rycenga, M.; Au, L.; Xia, Y. Isolating and Probing the Hot Spot Formed between Two Silver Nanocubes. *Angew Chemie Int. ed.* **2009**, *48*, 2180–2184.

[23] Banik, M.; El-Khoury, P. Z.; Nag, A.; Rodriguez-Perez, A.; Guarrottxena, N.; Bazan, G. C.; Apkarian, V. A. Surface-Enhanced Raman Trajectories on a Nano-Dumbbell: Transition from Field to Charge Transfer Plasmons as the Spheres Fuse. *ACS Nano* **2012**, *6*, 10343–10354.

[24] Banik, M.; Apkarian, V. A.; Park, T.-H.; Galperin, M. Raman Staircase in Charge Transfer SERS at the Junction of Fusing Nanospheres. *J. Phys. Chem. Lett.* **2013**, *4*, 88–92.

[25] Kleinman, S. L.; Sharma, B.; Blaber, M. G.; Henry, A.-I.; Valley, N.; Freeman, R. G.; Natan, M. J.; Schatz, G. C.; Van Duyne, R. P. Structure Enhancement Factor Relationships in Single Gold Nanoantennas by Surface-Enhanced Raman Excitation Spectroscopy. *J. Am. Chem. Soc.* **2013**, *135*, 301–308.

[26] Xu, H.; Aizpurua, J.; Kall, M.; Apell, P. Electromagnetic Contributions to Single-Molecule Sensitivity in Surface-Enhanced Raman Scattering. *Phys. Rev. E* **2000**, *62*, 4318–4324.

[27] Kelly, K. L.; Coronado, E.; Zhao, L. L.; Schatz, G. C. The Optical Properties of Metal Nanoparticles: The Influence of Size, Shape, and Dielectric Environment. *J. Phys. Chem. B* **2003**, *107*, 668–677.

[28] Blanco, L.; García-Vidal, F. Spontaneous Light Emission in Complex Nanostructures. *Phys. Rev. B* **2004**, *69*, 1–12.

[29] Nordlander, P.; Oubre, C.; Prodan, E.; Li, K.; Stockman, M. I. Plasmon Hybridization in Nanoparticle Dimers. *Nano Lett.* **2004**, *4*, 899–903.

[30] Chu, P.; Mills, D. Laser-Induced Forces in Metallic Nanosystems: The Role of Plasmon Resonances. *Phys. Rev. Lett.* **2007**, *99*, 1–4.

[31] Litz, J. P.; Camden, J. P.; Masiello, D. J. Spatial, Spectral and Coherence Maping of Single-Molecule Sers Active Hot Spots via the Discrete-Dipole Approximation. *J. Phys. Chem. Lett.* **2011**, *2*, 1695–1700.

[32] Song, P.; Nordlander, P.; Gao, S. Quantum Mechanical Study of the Coupling of Plasmon Excitations to Atomic-Scale Electron Transport. *J. Chem. Phys.* **2011**, *134*, 074701.

[33] Savage, K. J.; Hawkeye, M. M.; Esteban, R.; Borisov, A. G.; Aizpurua, J.; Baumberg, J. J. Revealing the Quantum Regime in Tunnelling Plasmonics. *Nature* **2012**, *491*, 574–577.

[34] Marinica, D. C.; Kazansky, a K.; Nordlander, P.; Aizpurua, J.; Borisov, a G. Quantum Plasmonics: Nonlinear Effects in the Field Enhancement of a Plasmonic Nanoparticle Dimer. *Nano Lett.* **2012**, *12*, 1333–1339.

[35] Scholl, J. a; García-Etxarri, A.; Koh, A. L.; Dionne, J. a. Observation of Quantum Tunneling between Two Plasmonic Nanoparticles. *Nano Lett.* **2013**, *13*, 564–569.

[36] Zhang, P.; Feist, J.; Rubio, A.; García-González, P.; García-Vidal, F. J. Ab Initio Nanoplasmonics: The Impact of Atomic Structure. *Phys. Rev. B - Condens. Matter Mater. Phys.* **2014**, *90*, 1–5.

[37] He, H. Y.; Pi, S. T.; Bai, Z. Q.; Banik, M.; Apkarian, V. A.; Wu, R. Q. Stark Effect and Nonlinear Impedance of the Asymmetric Ag-CO-Ag Junction: An Optical Rectenna. *J. Phys. Chem. C* **2016**, *120*, 20914–20921.

[38] Jiang, J.; Bosnick, K.; Maillard, M.; Brus, L. E. Single Molecule Raman Spectroscopy at the Junctions of Large Ag Nanocrystals. *J. Phys. Chem. B* **2003**, *107*, 9964–9972.

[39] Moore, A. a; Jacobson, M. L.; Belabas, N.; Rowlen, K. L.; Jonas, D. M. 2D Correlation Analysis of the Continuum in Single Molecule Surface Enhanced Raman Spectroscopy. *J. Am. Chem. Soc.* **2005**, *127*, 7292–7293.

[40] Itoh, T.; Biju, V.; Ishikawa, M.; Kikkawa, Y.; Hashimoto, K.; Ikehata, A.; Ozaki, Y. Surface-Enhanced Resonance Raman Scattering and Background Light Emission Coupled with Plasmon of Single Ag Nanoaggregates. *J. Chem. Phys.* **2006**, *124*, 134708.

[41] Otto, A.; Akemann, W.; Pucci, A. Normal Bands in Surface-Enhanced Raman Scattering (SERS) and Their Relation to the Electron-Hole Pair Excitation Background in SERS. *Isr. J. Chem.* **2006**, *46*, 307–315.

[42] Itoh, T.; Yoshida, K.; Biju, V.; Kikkawa, Y.; Ishikawa, M.; Ozaki, Y. Second Enhancement in Surface-Enhanced Resonance Raman Scattering Revealed by an Analysis of Anti-Stokes and Stokes Raman Spectra. *Phys. Rev. B* **2007**, *76*, 085405.

[43] Lombardi, J. R.; Birke, R. L. Excitation Profiles and the Continuum in SERS: Identification of Fano Line Shapes. *J. Phys. Chem. C* **2010**, *114*, 7812–7815.

[44] Galperin, M.; Nitzan, A. Raman Scattering from Biased Molecular Conduction Junctions: The Electronic Background and Its Temperature. *Phys Rev B* **2011**, *84*

[45] Hugall, J. T.; Baumberg, J. J. Demonstrating Photoluminescence from Au Is Electronic Inelastic Light Scattering of a Plasmonic Metal: The Origin of SERS Backgrounds. *Nano Lett.* **2015**, *15*, 2600–2604.

[46] Etchegoin, P. G.; Le Ru, E.; Meyer, M. An Analytic Model for the Optical Properties of Gold. *J. Chem. Phys.* **2006**, *12*, 164705.

[47] Olmon, R. L.; Slovick, B.; Johnson, T. W.; Shelton, D.; Oh, S. H.; Boreman, G. D.; Raschke, M. B. Optical Dielectric Function of Gold. *Phys. Rev. B.* **2012**, *86*, 235147.

[48] Dey, S.; Banik, M.; Hulkko, E.; Rodriguez, K.; Apkarian, V. A.; Galperin, M.; Nitzan, A. Observation and analysis of Fano-like lineshapes in the Raman spectra of molecules adsorbed at metal interfaces. *Phys. Rev. B* **2015**, *93*.

[49] Yang, W.-H.; Hulteen, J.; Schatz, G. C.; Van Duyne, R. P. A surface-enhanced hyper-Raman and surface-enhanced Raman scattering study of trans-1,2-bis(4-pyridyl)ethylene adsorbed onto silver film over nanosphere electrodes. Vibrational assignments: Experiment and theory. *J. Chem. Phys*. **1995**, 104.

[50] K. Kneipp, K.; Y. Wang, Y.; Kneipp, H.; Itzkan, I.; Dasari, R. R.; Feld, M. S. Population Pumping of Excited Vibrational States by Spontaneous Surface-Enhanced Raman Scattering. *Phys. Rev. Lett.* **1996**, *76*.

[51] Barron, L. D.; Hecht, L.; McColl, I. H.; Blanch, E. W. Raman optical activity comes of age. *Molec. Phys.* **2004**, *102*, 731-744.

[52] Atkins, P. W.; Baron, L. D. Rayleigh scattering of polarized photons by molecules. *Molec. Phys*. **1969**, *16*, 453-466.

[53] Efrati, E.; Irvine, W. T. M. Orientation-dependent handedness and chiral design. *Phys. Rev. X* **2014**, *4*, 1-12.

[54] Pham, A.; Jiang, Q.; Zhao, A.; Bellessa, J.; Genet, C.; Drezet, A. Manifestation of Planar and Bulk Chirality Mixture in Plasmonic Λ-Shaped Nanostructures Caused by Symmetry Breaking Defects. *ACS Photonics* **2017**, *4*, 2453-2460.

[55] Banik, M.; Rodriguez, K.; Hulko, E.; Apkarian, V. A. Orientation-dependent Handedness of Chiral Plasmons on Nanosphere Dimers: How to Turn a Right Hand into a Left Hand. *ACS Photonics* **2016**, *3*, 2482-2489.

[56] Kliger, D. S.; Lewis, J. W.; Randall, C. E. *Polarized Light in Optics and Spectroscopy*, 1st ed.; Academic
Press: Michigan, 1990.

[57] Raab, R. E.; de Lange, O. L. *Multipole Theory in Electromagnetism*, 1st ed.; Clarendon Press: Oxford,
2005.

[58] Tork-Ladani, F. *Electrodynamics of Illuminated Nanojunctions*; UC Irvine: Irvine, 2017.

[59] Jackson, J. D. *Classical Electrodynamics*; 3rd ed.; John Wiley & Sons, Inc., 1999.

[60] Kong, J. A. *Electromagnetic Waves Theory*; EMW: Cambridge, MA 2008.

[61] Veselago, V. G. Electrodynamics of substances with simultaneously negative electrical and magnetic
permeabilities. *Soviet Physiks Uspehki* **1968**, 10, 509-514.

[62] Hecht, E. *Optics*, 4th ed.; Pearson: Essex, 2012.

[63] Pendry, J. B. Negative refraction makes a perfect lens. *Phys. Rev. Lett.* **2000**, *85*, 3966-3969.

[64] From: https://skullsinthestars.com/2009/05/19/what-does-negative-refraction-look-like/. Accessed Jan. 2019.

[65] Capolino, F. *Theory and Phenomena of Metamaterials*; CRC Press: New York, 2009.

[66] Pendry, J. B. Low frequency plasmons in thin-wire structures. *J. of Phys.: Cond. Matt*. **1998**, *10*, 4785-4809

[67] Ramakrishna, S. A. Physics of negative refractive index materials. *Rep. Prog. Phys.* **2005**, *68*, 449-521.

[68] Pendry, J. B. New electromagnetic materials that emphasize the negative. From: http://www.cmth.ph.ic.ac.uk/photonics/Newphotonics/pdf/pw2article.pdf. Accessed Jan. 2019.

[69] Smith, D. RR.; Padilla, W. J.; Vier, D. C.; Nemat-Nasser, S. C.; Schultz, S. Composite medium with
simultaneously negative permeability and permittivity. *Phys. Rev. Lett*. **2000**, *84*, 4181-4187.

[70] Panina, L. V.; Grigorenko, A. N.; Makhnovsky, D. P. Optomagnetic composite medium with conducting
nanoelements. *Phys. Rev. B* **2002**, *66*, 1-17.

[71] Hsu, Y.-J.; Huang, Y.-C.; Lih, J.-S.; Chern, J.-Y. ELectromagnetic resonance in deformed split ring
resonators of left-handed meta-materials. *J. App. Phys*. **2004**, *96*, 1979-1982.

[72] Kamenetskii, E.; Sigalov, M.; Shavit, R. Do the Tellegen particles really exist in electromagnetics? From: https://arxiv.org/ftp/arxiv/papers/0807/0807.4280.pdf. Accessed Jan. 2019.

[73] Born, M.; Wolf E. *Principles of Optics*, 7th ed.; Pergamon Press Ltd: Cambridge, MA 2011.

[74] Landau, L. D.; Lifshitz, E. M. *Electrodynamics of Continuous Media*; Butterworth-Heinemann: Oxford, 1984; Chapter 9.

[75] Efrima, S. The Effect of Large Electric Field Gradients on the Raman Optical Activity of Molecules adsorbed on Metal Surfaces. *Chem. Phys. Lett*. **1983**, *102*, 79−82.

[76] Jensen, L. Surface-Enhanced Vibrational Raman Optical Activity: A Time-Dependent Density Functional Theory Approach*. J. Phys. Chem. A* **2009**, *113*, 4437−4444.

[77] Acevedo, R.; Lombardini, R.; Halas, N. J.; Johnson, B. R. Plasmonic Enhancement of Raman Optical Activity in Molecules near Metal Nanoshells*. J. Phys. Chem. A* **2009**, *113*, 13173−13183.

[78] Govorov, A. O.; Fan, Z.; Hernandez, P.; Slocik, J. M.; Naik, R. R. Theory of Circular Dichroism of Nanomaterials Comprising Chiral Molecules and Nanocrystals: Plasmon

Enhancement, Dipole Interactions, and Dielectric Effects. *Nano Lett.* **2010**, *10*, 1374−1382.